Biochemistry

pubs.acs.org/biochemistry Article

Mechanism of the Multistep Catalytic Cycle of 6-Hydroxynicotinate 3-Monooxygenase Revealed by Global Kinetic Analysis

Scott W. Perkins, May Z. Hlaing, Katherine A. Hicks, Lauren J. Rajakovich,* and Mark J. Snider*

Cite This: *Biochemistry* 2023, 62, 1553−1567 Read Online

ABSTRACT: The class A flavoenzyme 6-hydroxynicotinate 3-monooxygenase (NicC) catalyzes a rare decarboxylative hydroxylation reaction in the degradation of nicotinate by aerobic bacteria. While the structure and critical residues involved in catalysis have been reported, the mechanism of this multistep enzyme has yet to be determined. A kinetic understanding of the NicC mechanism would enable comparison to other phenolic hydroxylases and illuminate its bioengineering potential for remediation of *N*-heterocyclic aromatic compounds. Toward these goals, transient state kinetic analyses by stopped-flow spectrophotometry were utilized to follow rapid changes in flavoenzyme absorbance spectra during all three stages of NicC catalysis: (1) 6-HNA binding; (2) NADH binding and FAD reduction; and (3) O_2 binding with C4a-adduct formation, substrate hydroxylation, and FAD regeneration. Global kinetic simulations by numeric integration were used to supplement analytical fitting of time-resolved data and establish a kinetic mechanism. Results indicate that 6-HNA binding is a two-step process that substantially increases the affinity of NicC for NADH and enables the formation of a charge-transfer-complex intermediate to enhance the rate of flavin reduction. Singular value decomposition of the time-resolved spectra during the reaction of the substrate-bound, reduced enzyme with dioxygen provides evidence for the involvement of C4a-hydroperoxy-flavin and C4a-hydroxy-flavin intermediates in NicC catalysis. Global analysis of the full kinetic mechanism suggests that steady-state catalytic turnover is partially limited by substrate hydroxylation and C4a-hydroxy-flavin dehydration to regenerate the flavoenzyme. Insights gleaned from the kinetic model and determined microscopic rate constants provide a fundamental basis for understanding NicC's substrate specificity and reactivity.

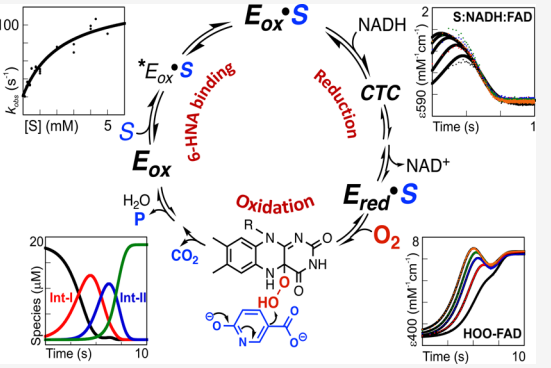

INTRODUCTION

Natural and anthropogenic *N*-heterocyclic aromatic compounds (*N*HACs) are pervasive toxic chemicals in the environment of public health concern.[1,2] Several strains of common soil bacteria catabolize *N*HACs to core metabolic intermediates via pathways beginning with aromatic ring hydroxylation catalyzed by dehydrogenases and monooxygenases.[3−5] Nicotinate catabolism serves as a model for understanding the mechanistic strategies bacteria use to degrade *N*HACs.[6] Despite being a model pathway for *N*HAC degradation, biochemical characterization of the enzymes involved in aerobic nicotinate catabolism is limited.[7−10] A deeper structural and kinetic understanding of the mechanism and substrate specificity achieved particularly by the ring-hydroxylating enzymes would serve to enhance bioengineering and bioremediation efforts.[11,12]

The key aromatic hydroxylation step in aerobic nicotinate degradation is catalyzed by 6-hydroxynicotinate 3-monooxygenase (NicC; EC:1.14.13.114). NicC uses the flavin cofactor FAD to activate dioxygen and transfer one oxygen atom, as a hydroxyl group, to C3 of the nicotinate ring. Subsequent decarboxylation of the resulting tetrahedral intermediate at C3 is driven by re-aromatization of the ring and forms the final product, 2,5-dihydroxypyridine (2,5-DHP).[13] Thus, NicC catalyzes both hydroxylation and decarboxylation of 6-hydroxynicotinate (6-HNA) with stoichiometric oxidation of NADH to NAD^+ (Figure 1A).

Studies of single-component class A flavin monooxygenases that hydroxylate phenolic substrates have elucidated the canonical steps in catalysis (for recent reviews, see refs 14−20). The multiple enzymatic reactions precisely orchestrated at one active site can be organized into three segments: (i) substrate binding, (ii) the reductive half-reaction, and (iii) the oxidative half-reaction. In the first segment, the aromatic substrate and NAD(P)H bind in an ordered or random fashion to create a ternary complex (Figure 1B, step 1). The second segment involves NAD(P)H binding and hydride transfer from NAD(P)H to FAD (Figure 1B, step 2). Upon $NAD(P)^+$

Received: September 1, 2022
Revised: April 10, 2023
Published: May 2, 2023

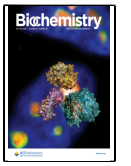

https://doi.org/10.1021/acs.biochem.2c00514
Biochemistry 2023, 62, 1553−1567

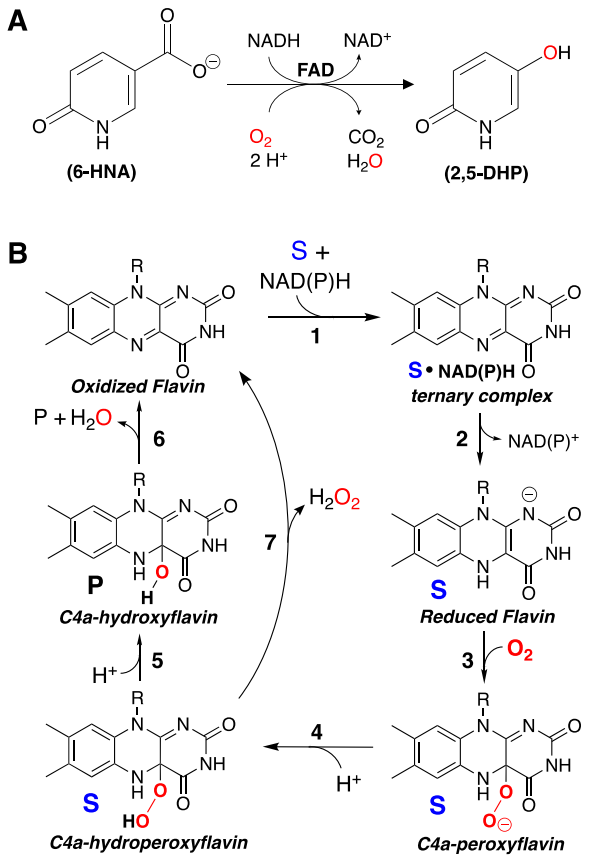

Figure 1. Flavin-dependent aromatic ring hydroxylation in bacterial degradation pathways. (A) Hydroxylation and decarboxylation of 6-hydroxynicotinate (6-HNA) to 2,5-dihydroxypyridine (2,5-DHP) catalyzed by the FAD-dependent monooxygenase, NicC. (B) Flavin intermediates typically observed in the catalytic cycle of class A flavin-dependent monooxygenases. R = adenine dinucleotide for FAD; S = aromatic substrate; P = hydroxylated product.

dissociation from the enzyme, the reduced flavin reacts with dioxygen in the third segment (Figure 1B, steps 3−6). Dioxygen reduction results in its adduction at C4a of the flavin isoalloxazine ring, forming either a stable C4a-peroxy-flavin or C4a-hydroperoxy-flavin intermediate. The terminal hydroxyl group of the (hydro)peroxy-flavin intermediate is transferred to the aromatic substrate, resulting in C4a-hydroxy-flavin and the final hydroxylated product or a hydroxylated intermediate that undergoes additional transformations. The oxidized flavin cofactor is then regenerated upon dehydration of the C4a-hydroxy-flavin intermediate. In a small fraction of events, the C4a-hydroperoxy-flavin intermediate can also decay to release hydrogen peroxide, resulting in "unproductive" flavin regeneration without substrate hydroxylation (Figure 1B, step 7).

Compared to flavin-dependent phenol hydroxylases, monooxygenases that catalyze hydroxylation of pyridinolic substrates are poorly characterized. Moreover, hydroxylation of an atom already bearing a substituent on an aromatic ring, causing the substituent to migrate or depart (an *ipso* substitution), is rare among flavin-dependent aromatic ring hydroxylases. NicC is one of only six enzymes, including 5-hydroxypicolinic acid 2-monooxygenase (HpaM),[21] 6-hydroxy-3-succinoyl-pyridine 3-monooxygenase (HspB),[22] 2-methyl-3-hydroxypyridine-5-carboxylate oxygenase (MHPCO),[23] 5-methylphenazine-1-carboxylate 1-monooxygenase (PhzS),[24] and indole-3-carboxylate monooxygenase (ICM),[25] that are known to catalyze hydroxylation and C−C cleavage at the same position of a heterocyclic substrate (Figure S1). Among these monooxygenases, only MHPCO[23] and HspB[22] have been described in any kinetic detail. We recently reported the crystal structure of the flavin-bound *Pseudomonas putida KT2440* NicC enzyme[10] (PDB 5EOW) and provided evidence from steady state kinetic analysis of active site variants to identify the residues important in the catalytic mechanism of the *Bordetella bronchiseptica RB50* NicC homologue.[13] Given the low sequence conservation (<30% identity) among the enzymes predicted to be structurally similar to NicC[10] and the results of our earlier investigation showing that active site conservation between these monooxygenases does not necessarily predict the key catalytic residues,[13] detailed biochemical investigations are warranted to address mechanistic differences and inform biotechnological applications.

In the current work, we determined the kinetic mechanism of NicC in each stage of catalysis − substrate binding, flavin reduction by NADH, and flavin oxidation with concomitant substrate hydroxylation − using stopped-flow UV−visible absorption spectroscopy. Global simulations of the data revealed the microscopic rate constants and spectral features of intermediate states in substrate binding, FAD reduction, and oxidation, including the key flavin C4a-oxygen adduct intermediates during catalysis. Results of these kinetic investigations provide insight on the steps contributing to the catalytic rate of NicC and enable a comparison between the catalytic mechanisms of flavoenzymes that hydroxylate phenolic and pyridinolic substrates. Moreover, the resulting kinetic model of NicC with 6-HNA provides a basis for future understanding reactivity with alternative substrates necessary to explore its bioengineering potential.

MATERIALS AND METHODS

Enzyme Expression and Purification. The cloning of the *nicC* gene from *Bordetella bronchiseptica RB50* into the pET-based expression vector pTHT for recombinant expression and purification of the *N*-His_6-NicC enzyme from *E. coli* BL21-(DE3) was described previously.[10] Concentrated fractions containing enzyme from HisTrap HP (GE Life Sciences) were buffer exchanged using 10DG desalting column (Bio-Rad) into gel filtration buffer [Tris (50 mM), NaCl (100 mM), DTT (2 mM), pH 7.5] and were further purified to homogeneity using a HiLoad 16/600 Superdex 75 pg column (GE Life Sciences). Purified fractions were concentrated by centrifugation (YM-10 Amicon ultrafiltration 10 kDa), buffer exchanged by desalting into storage buffer [Tris (20 mM, pH 7.2), NaCl (100 mM), glycerol (25%, v/v), EDTA (0.1 mM), and DTT (2 mM)], and flash frozen in liquid N_2 to be stored at −80 °C. The day before functional analyses, enzyme stocks were thawed and incubated with excess FAD overnight at 4 °C. Immediately prior to functional analysis, the enzyme solution was desalted (BioRad 10DG column) to exchange the enzyme into reaction buffer [sodium phosphate (50 mM, pH 7.5)] and remove unbound FAD. FAD-bound (active) NicC concentrations were determined by absorbance using the previously determined extinction coefficient (ε_{450} = 11,900 $M^{-1}\cdot cm^{-1}$).[10]

Equilibrium Binding of 6-HNA. Separate solutions of NicC (0.5 mL; either 19, 40, or 55 μM) in sodium phosphate buffer (50 mM, pH 7.5) were titrated by stepwise additions of a solution of 6-HNA (1.0 or 2.0 mM) in the same buffer at 4 °C in duplicate in two sample cells. The changes in absorbance

https://doi.org/10.1021/acs.biochem.2c00514
Biochemistry 2023, 62, 1553−1567

at 450 nm (A_{450}) were measured using a dual beam spectrophotometer. The absorbance values were corrected for dilution and baseline corrected by subtracting the absorbance at 700 nm. The ΔA_{450} was determined by subtracting the A_{450} of substrate-free enzyme from the final A_{450} after equilibration (3 min) with the substrate and then was normalized by the enzyme concentration to give the $\Delta\varepsilon_{450}$ for each substrate concentration. Using KaleidaGraph (v4.5), the average $\Delta\varepsilon_{450}$ of two replicates was fit as a function of 6-HNA concentration with eq 1.1 and eq 1.2 to determine the K_d of the E_{ox}·6-HNA complex:

$$\Delta\varepsilon_{450,obs} = (\varepsilon_{ES} - \varepsilon_E)\left[\frac{(E_0 + S_0 + K_{d,net}) - \sqrt{(E_0 + S_0 + K_{d,net})^2 - 4\cdot E_0\cdot S_0}}{2\cdot E_0}\right] \quad (1.1)$$

$$\Delta\varepsilon_{450,obs} = (\varepsilon_{ES} - \varepsilon_E)\left(\frac{1}{1 + ({}^{K_{d,net}}/_{S}) + ({}^{S}/_{K_{d,2}})}\right) \quad (1.2)$$

Stopped-Flow Absorption Spectroscopy. Rapid mixing experiments were carried out using an Applied Photophysics Ltd. (Leatherhead, UK) SX20 stopped-flow spectrophotometer housed in an anaerobic vinyl chamber (Coy Laboratory Products, Inc., USA). Reaction temperature was maintained at 4 °C using a circulating water bath. Atmospheric oxygen levels were maintained at 0−5 ppm using a palladium catalyst and H_2:N_2 (5:95) gas mix during all stopped-flow experiments. The instrument was configured for single-mixing, an optical pathlength of 1 cm, and data acquisition with a photodiode-array (PDA) detector. Time-dependent absorbance spectra (1000 points) were acquired with a split- or logarithmic-time base.

Anaerobic Solution Preparations. The stopped-flow spectrophotometer was scrubbed of O_2 by washing both mixing syringes and lines with sodium dithionite (10 mL of 10 mM) followed by O_2-free water (10 mL) and then O_2-free reaction buffer (10 mL). All rapid-mixing experiments were conducted at 4 °C in reaction buffer composed of sodium phosphate made by combining solutions of NaH_2PO_4 (0.20 M) and Na_2HPO_4 (0.20 M), titrating the solution pH to 7.5 by addition of NaOH (3 M), and diluting to the final working concentration (0.050 M). Enzyme solutions in reaction buffer (2−4 mL) were deoxygenated by cycling vacuum and N_2 (*g*) eight times on a dedicated Schlenk line in a reaction flask on ice and then brought into the anaerobic chamber. The concentration of FAD-bound enzyme solutions was determined by absorbance at 450 nm (ε_{450} = 11,900 $M^{-1}\cdot cm^{-1}$) and diluted with anaerobic reaction buffer to assay-specific concentrations inside the anaerobic chamber. Reaction buffer and stocks of 6-HNA (approx. 25 mM) in reaction buffer were deoxygenated by three freeze−pump−thaw cycles on a Schlenk line. The pressure measured during the third pump reached <50 mTorr. NADH solutions were made by dissolving crystalline NADH in the chamber with anaerobic reaction buffer. Concentrations of stock solutions of 6-HNA and NADH were determined by absorbance using the extinction coefficients ε_{295} = 5700 $M^{-1}\cdot cm^{-1}$ and ε_{340} = 6220 $M^{-1}\cdot cm^{-1}$, respectively. Solutions of saturated O_2 were made by bubbling 50 mM sodium phosphate (pH 7.5) reaction buffer within a sealed reaction flask containing a septum and needle in an ice bath with 100% O_2 (*g*) for ∼1 h. Sealed oxygen-saturated solutions were brought into the anaerobic chamber and diluted with cold anaerobic reaction buffer to achieve the desired O_2 concentration immediately before use and kept at 4 °C using a cold block.

Kinetics of 6-HNA Binding by NicC. Using the stopped-flow instrument equilibrated at 4 °C, oxidized NicC (92 μM in reaction buffer in syringe A) was mixed with an equal volume of 6-HNA solutions of different concentrations (0.2−14 mM in reaction buffer in syringe B). Absorbance spectra (n = 1000) were collected from 250−721 nm over a timeframe of 0.001−1 s using a photodiode array detector. The absorbance values at 450 nm (A_{450}) and 476 nm (A_{476}) were baseline-corrected by subtracting the absorbance at 721 nm (A_{721}) at each time point. The baseline-corrected absorbance values from 3−4 replicates were averaged and fit with a single exponential equation (eq 2) using *KaleidaGraph* v4.5.

$$A(t) = A_0 + \Delta A(1 - e^{-k_{obs}t}) \quad (2)$$

The k_{obs} values from two independent experiments as a function of substrate concentration were fit with a hyperbolic equation (eq 3) using *KaleidaGraph* v4.5.

$$k_{obs} = \frac{k_2({}^{S}/_{K_{d,1}})}{1 + ({}^{S}/_{K_{d,1}})} + k_{-2} \quad (3)$$

The time-dependent traces were also fit by simulation, as described below.

Kinetics of NicC Reduction by NADH. In experiment #1, an anoxic solution of oxidized NicC (44 μM, syringe A) was rapidly mixed in an equal volume with anoxic solutions of NADH (0.25−20 mM in syringe B) at 4 °C, using the stopped-flow instrument. The absorbance spectra from 250−721 nm were collected over a time frame of 0.001−10 s or 0.01−100 s using a diode array detector. The A_{450} values were baseline-corrected by subtracting the absorbance at 721 nm at each time point. The baseline-corrected, average A_{450} values of at least three replicates were plotted as a function of time and fit by nonlinear regression using an equation with three consecutive exponential functions (eq 4). The observed rate constants were plotted as a function of NADH concentration and fit using eq 3.

$$A(t) = A_0 + \Delta A_a(1 - e^{(-k_a t)}) + \Delta A_b(1 - e^{(-k_b t)}) + \Delta A_c(1 - e^{(-k_c t)}) \quad (4)$$

In experiment #2, an anoxic solution of oxidized NicC (40 μM) and 6-HNA (2.5 mM) was pre-incubated and loaded into syringe A. Solutions of NADH (0.01−0.8 mM, syringe B) in anoxic reaction buffer were then rapidly mixed in an equal volume with syringe A at 4 °C, using the stopped-flow instrument. Absorbance spectra (n = 1000) from 250−721 nm were collected over a time frame of 0.001−1 s using a diode array detector. The absorbance values at 450 nm (A_{450}) and 590 nm (A_{590}) were baseline-corrected by subtracting the absorbance at 721 nm at each time point and averaged from three replicates. The baseline-corrected, averaged A_{450} and A_{590} time-dependent traces were fit by nonlinear regression using a double exponential equation (eq 5).

$$A(t) = A_0 + \Delta A_a(1 - e^{(-k_a t)}) + \Delta A_b(1 - e^{(-k_b t)}) \quad (5)$$

In experiment #3, an anoxic solution of oxidized NicC (5 μM) was preincubated with 6-HNA (2.5 mM) in syringe A. This solution was rapidly mixed with an equal volume of a

https://doi.org/10.1021/acs.biochem.2c00514
Biochemistry 2023, 62, 1553−1567

solution of NADH (0.01−0.4 mM) in syringe B at 4 °C, using a stopped-flow instrument. The absorbance spectra were collected from 250−721 nm over a time frame of 0.001−1 s using a photodiode array detector. The A_{450} values were baseline-corrected by subtracting the absorbance at 721 nm and averaged using three or four replicates. The time-dependent traces were fit by nonlinear regression using a double exponential equation (eq 5) and by simulation as described below.

Kinetics of Reduced NicC Reacting with NAD. An O_2-free solution of 0.040 mM NicC, 0.04 mM NADH, and 2.5 mM 6-HNA was prepared in reaction buffer and loaded into syringe A. An O_2-free solution of 20 mM NAD^+ was loaded into syringe B. Syringes A and B were rapidly mixed 1:1, and the absorbance spectra (n = 1000) were measured using a logarithmic timescale for 120 or 1000 s. This assay was replicated in the absence of 6-HNA. Absorbance values at 450 and 590 nm were baseline-corrected by subtracting the absorbance at 721 nm at each time point and averaged from at least three replicates.

Kinetics of Reduced NicC Reacting with Dioxygen. An O_2-free solution of 0.04 mM NicC, 0.04 mM NADH, and 2.5 mM 6-HNA was prepared in reaction buffer and loaded into syringe A. Chilled (4 °C) O_2-saturated (~1.9 mM) reaction buffer was diluted with chilled anoxic reaction buffer in ratios that yielded O_2 concentrations of 0.24, 0.48, 0.96, 1.44, or 1.9 mM immediately before loading syringe B. Syringes A and B were rapidly mixed 1:1, and the absorbance spectra (n = 1000) were measured using a split timescale (800 points from 0−0.8 s, 200 points from 0.8−10 s). This assay was replicated in the absence of 6-HNA at a single O_2 concentration (1.9 mM in syringe B). To measure the effects of azide, a solution of 0.040 mM NicC, 0.040 mM NADH, 2.5 mM 6-HNA, and 50 mM NaN_3 in anoxic reaction buffer was rapidly mixed with an equal volume of chilled O_2-saturated (1.9 mM) reaction buffer containing 50 mM NaN_3 in the stopped-flow instrument. To determine the effect of high concentrations of the 2,5-dihydropyridine product, a solution of 0.040 mM NicC, 0.040 mM NADH, 2.5 mM 6-HNA, and 10 mM 2,5-DHP in anoxic reaction buffer was rapidly mixed with an equal volume of chilled O_2-saturated (1.9 mM) reaction buffer in the stopped-flow instrument.

Absorbance values at 349, 400, and 450 nm were baseline-corrected by subtracting the absorbance at 721 nm at each time point and averaged from at least three replicates. The baseline-corrected time-dependent traces were fit by nonlinear regression using equations derived from a three-step irreversible kinetic model (shown below):

$$A \xrightarrow{k_1} B \xrightarrow{k_2} C \xrightarrow{k_3} D$$

where k_1 corresponds to the pseudo-first-order rate constant $k[O_2]$ when O_2 is in sufficient excess of enzyme (>2-fold). Equation 6 was used to fit the A_{349} and A_{400} time-dependent traces, assuming that all four states absorb at these wavelengths with different extinction coefficients (eq 7).

$$\Delta A(t) = y.\text{int} + \Delta A_{(A-D)}\, e^{-k_1 t} + \Delta A_{(B-D)}\frac{k_1}{k_2 - k_1}(e^{-k_1 t} - e^{-k_2 t}) + \Delta A_{(C-D)}\frac{k_2 k_1}{k_2 - k_1}\left(\frac{1}{k_3 - k_1}(e^{-k_1 t} - e^{-k_3 t}) - \frac{1}{k_3 - k_2}(e^{-k_2 t} - e^{-k_3 t})\right) \quad (6)$$

$$\Delta A = \varepsilon_A[A] + \varepsilon_B[B] + \varepsilon_C[C] + \varepsilon_D[D] \quad (7)$$

The A_{450} time-dependent traces were fit using eq 8, which assumes that the absorbance contributed by states A, B, and C at this wavelength is negligible.

$$\Delta A(t) = y.\text{int} + \Delta A_D\left\{1 - e^{-k_1 t} + \frac{k_1}{k_2 - k_1}(e^{-k_1 t} - e^{-k_2 t}) - \frac{k_2 k_1}{k_2 - k_1}\left(\frac{1}{k_3 - k_1}(e^{-k_1 t} - e^{-k_3 t}) - \frac{1}{k_3 - k_2}(e^{-k_2 t} - e^{-k_3 t})\right)\right\} \quad (8)$$

The A_{349}, A_{400}, and A_{450} time-dependent traces were also simulated as described below.

Kinetic Data Analysis by Simulation. Data simulations were performed using KinTek Global Kinetic Explorer v8.0.[26] The time-dependent traces analyzed were the baseline-corrected averages of at least three replicates. The sigma values for each data point were the standard deviation calculated from the three replicates. The simulated observables were defined to represent the sum of the absorbance of each species based on the extinction coefficient (ε) at that wavelength. Extinction coefficients were treated as independent variables, except for species for which the absorbance spectrum could be measured separately. The data were simulated, using numerical integration of the rate equations corresponding to a given kinetic model, to determine a set of "best-fit" parameters that achieve a minimum χ^2 value by nonlinear regression. Statistical analyses (1D) were performed using KinTek FitSpace Explorer[27] with the threshold set to a value of 0.67 for the minimum χ^2/χ^2 value. In this 1D analysis, the χ^2 was calculated at set values of each parameter while allowing all other variables to float over a range of 0.01× to 10× the best-fit value. Upper and lower limits for each parameter were determined using a threshold of 0.95 (minimum χ^2/χ^2), equivalent to a 95% confidence interval.

Substrate Binding. Global simulation was used to fit the data at four wavelengths (349, 400, 450, and 476 nm) based on a two-site kinetic model (Scheme 1B). The extinction coefficients for E_{ox} and S at 450 and 476 nm were held constant. The extinction coefficients for E_{ox} and $^*E_{ox}$·S were linked to be equivalent.

Reductive Half-Reaction. Simulation was used to fit the data at 450 nm without substrate based on a three-step or four-step (Scheme 2A) kinetic model. The extinction coefficient for E_{ox} was held constant. Comparison of the residuals between the simulation and the data and calculation of the χ^2 indicated a better simulation using the four-step model. Global simulation was used to fit four sets of data from three experiments: (1) A_{450} traces for FAD reduction without

https://doi.org/10.1021/acs.biochem.2c00514
Biochemistry 2023, 62, 1553−1567

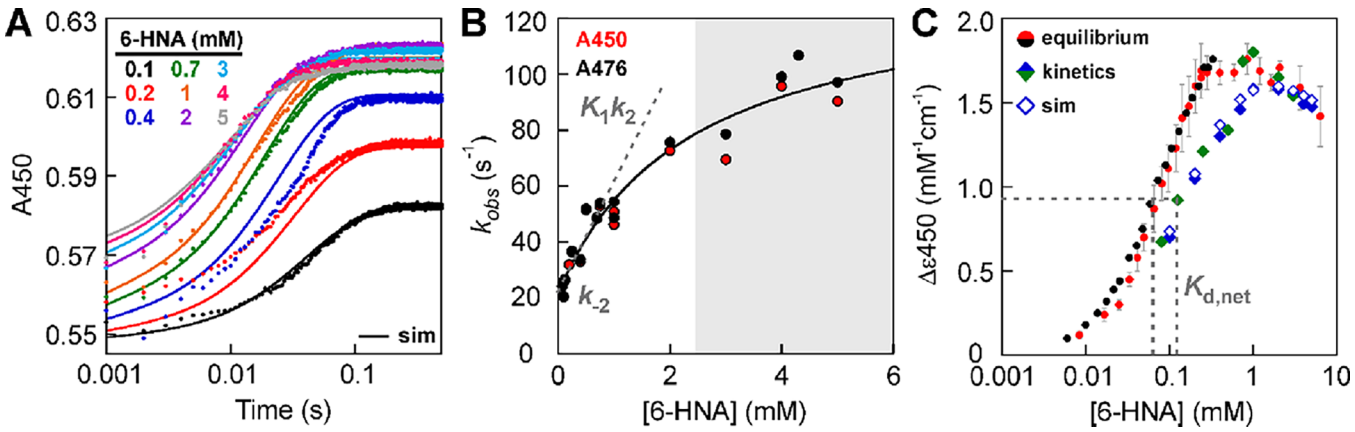

Figure 2. Transient state kinetics demonstrate rapid equilibrium, two-step binding of 6-HNA to oxidized NicC (E_{ox}) at 4 °C. (A) A_{450} time-dependent traces obtained from mixing solutions of 6-HNA (final concentrations listed) with an equal volume of E_{ox} (46 μM, final). Data points are triplicate averages and solid lines represent simulations using the kinetic model shown in Scheme 1B. (B) Hyperbolic fit of the observed rate constants obtained from analytical fits of the A_{450} and A_{476} time-dependent traces with varying 6-HNA concentrations (Figure S3). Gray background denotes concentrations of 6-HNA resulting in decreased apparent final A_{450}. (C) Change in the NicC extinction coefficient at 450 nm compared to free E_{ox} as a function of total 6-HNA concentration. Circles represent two independent equilibrium titrations with 40 μM NicC (black) and 19 μM NicC (red). Diamonds represent two independent kinetics experiments with 46 μM NicC (blue) and 37 μM NicC (green). Empty diamonds represent the $\Delta\varepsilon_{450}$ values from the simulations shown in panel A.

substrate, (2) A_{450} traces for FAD reduction with substrate at low enzyme concentration, and (3) A_{450} and A_{590} traces for FAD reduction with the substate at high enzyme concentration. The kinetic model for substrate binding was included with fixed extinction coefficients and rate constants. The four-step kinetic model for FAD reduction in the absence of substrate was used with fixed extinction coefficients for the E_{ox}·NADH complexes based on the simulation of the data without substrate alone. A three-step kinetic model was used for FAD reduction in the presence of substrate (Scheme 2B). The extinction coefficients for E_{ox}, E_{red}·S·NAD^+, and E_{red}·S at 590 nm were linked to be equivalent. Thermodynamic cycles for 6-HNA binding, FAD reduction, and NAD^+ dissociation were constrained to unity.

Oxidative Half-Reaction. Global simulation was used to fit the data at three wavelengths (349, 400, 450 nm) and a set of time-resolved spectra based on a kinetic model with four sequential steps and one step representing an off-pathway reaction (Scheme 3B). The kinetic model, extinction coefficients, and rate constants for substrate binding and FAD reduction in the presence and absence of substrate were fixed. The ratio of k_7:k_{7a} was fixed at 9:1 based on the results of the observed stoichiometry of 2,5-DHP and H_2O_2 formation. A singular value decomposition (SVD) analysis with four Eigenvectors was performed with the time-resolved spectra using the same kinetic model.

Multiple Turnover Reaction. The steady state, multiple turnover reactions were simulated (not fit) based on the global kinetic model and rate constants for substrate binding, the reductive half-reaction (with and without substrate), and the oxidative half-reaction. Reactions accounting for the decomposition of NADH and the oxidative half-reaction in the absence of substrate (Scheme 3A) were also included in the global kinetic model.

Stoichiometry of 2,5-DHP and H_2O_2 Formation. Five replicates of O_2-free solutions (0.25 mL) containing 0.04 mM oxidized NicC, 2.5 mM 6-HNA, and 0.04 mM NADH in reaction buffer (50 mM sodium phosphate, pH 7.5) were prepared in the anaerobic chamber at 4 °C. Each solution was mixed with an equal volume of cold O_2 saturated (1.9 mM) reaction buffer and incubated at 4 °C for 3 min. The reaction solutions were filtered by centrifugation (Amicon 10 kDa centrifugal ultrafiltration) at 4 °C for 15 min to remove the enzyme prior to hydrogen peroxide and product quantitation. An aliquot from each reaction was then injected (10 μL), and the resulting products were separated by HPLC using a C18 column (2.6 μm, 100 × 2.1 mm) following a previously published procedure.[13] The concentration of 2,5-DHP was determined in each sample by comparing the integrals of the resolved eluted peaks to the instrument's linear response to a set of standards analyzed within the same batch run. Separate aliquots (100 μL) from the filtered reaction samples were also analyzed for their concentration of hydrogen peroxide using the Qubit Fluorometer Amplex Red Assay (Invitrogen). A standard curve of hydrogen peroxide (0−25 μM) with the Amplex Red reagent was prepared, and the fluorescence signal was measured at 590 nm (Figure S2) using a Qubit 4 fluorometer (Invitrogen) with an excitation wavelength of 570 nm. The signal intensity was observed to be suppressed in the presence of 2,5-DHP. To account for this effect in analysis of the product samples, the concentration of hydrogen peroxide was determined from the standard curve measured in the presence of multiple 2,5-DHP concentrations (10, 20, 30, 50 μM).

Steady-State Kinetic Measurements. Steady-state kinetic parameters were determined from initial rates measured by following the decrease in absorbance at 340 nm ($\Delta\varepsilon$ = 6220 M^{-1} cm^{-1}) upon oxidation of NADH in sodium phosphate buffer (50 mM, pH 7.5) using a constant concentration of wild-type NicC. The turnover number ($v/[E_o]$) was determined from A_{340} measurements over 1000 s from reactions containing 20 nM oxidized NicC, 0.1 mM NADH, and 0.1 mM 6-HNA in chilled (~0.4 mM O_2) 50 mM sodium phosphate buffer, pH 7.5 at 4 °C. Reactions omitting 6-HNA contained 1 μM oxidized NicC and 0.1 mM NADH in 50 mM sodium phosphate buffer (pH 7.5) were monitored for 100 min at 4 °C. Decomposition of NADH (0.093 mM) in the

https://doi.org/10.1021/acs.biochem.2c00514
Biochemistry 2023, 62, 1553−1567

absence of enzyme in 50 mM sodium phosphate buffer (pH 7.5) at 4 °C was monitored for 50 min.

Inhibition kinetics with the product 2,5-DHP were measured at 4 °C at 380 nm ($\Delta\varepsilon$ = 1229 M^{-1} cm^{-1}) in two assays in which the concentration of 2,5-DHP was held constant at either 0, 0.75, 1.5, or 3.0 mM with 200 nM oxidized NicC in 50 mM sodium phosphate buffer (pH 7.5). In the first assay, rates were measured using a constant concentration of NADH (0.10 mM) and varying the concentration of 6-HNA (0.012−3.0 mM). In the second assay, 6-HNA concentration was held constant (0.50 mM) and the concentration of NADH was varied (4−50 μM) with 2,5-DHP concentration set at 0 or 3.0 mM. Initial rates were fit globally using inhibition models in GraFit (v6, Erithacus Software Limited) to determine the mode of inhibition and K_i values for 2,5-DHP.

RESULTS

Binding of 6-HNA to Oxidized NicC Is a Two-Step Process. We first sought to determine the equilibrium and rate constants for 6-HNA substrate binding by rapid-mixing kinetics. We previously reported that binding of 6-HNA to oxidized NicC (E_{ox}) perturbed the UV−visible absorbance spectrum of the enzyme-bound FAD cofactor (Figure S3).[13] Using a stopped-flow spectrophotometer, the change in absorbance at 450 nm (A_{450}) and 476 nm (A_{476}) was monitored over time after rapidly mixing 6-HNA with E_{ox} at 4 °C (Figure 2A and Figure S3). The A_{450} and A_{476} time-dependent traces were fit by nonlinear regression with a single exponential equation (Figure S3). The observed pseudo-first-order rate constants (k_{obs}) demonstrated non-linear dependence on the concentration of 6-HNA (Figure 2B), indicating a two-step binding mechanism (Scheme 1A). In this model, a rapid equilibrium establishes an initial $*E_{ox}$·6-HNA complex ($*E_{ox}$·S), which is reflected in the data by higher initial A_{450} values (t = 0.001 s) with increasing 6-HNA concentrations (Figure 2A). This substrate-enzyme complex then converts to a distinct E_{ox}·6-HNA state (E_{ox}·S) that has a substantially higher extinction coefficient at 450 nm (Figure 2A) and 476 nm (Figure S3). The hyperbolic fit (eq 3) of the k_{obs} values from the A_{450} and A_{476} time-dependent traces (Figure 2B) provided estimates of the initial dissociation constant (K_{d1} = 2.3 mM) and the microscopic rate constants (k_2 = 110 s^{-1} and k_{-2} = 21 s^{-1}) (Table 1).

Scheme 1. Kinetic Models for Substrate Binding with One Site (A) or Two Sites (B)

A One-site model

$$E_{ox} + S \overset{K_{d,1}}{\rightleftharpoons} {}^*E_{ox}{\bullet}S \overset{k_2}{\underset{k_{-2}}{\rightleftharpoons}} E_{ox}{\bullet}S$$

B Two-site model

$$E_{ox} + S \overset{K_{d,1}}{\rightleftharpoons} {}^*E_{ox}{\bullet}S \overset{k_2}{\underset{k_{-2}}{\rightleftharpoons}} E_{ox}{\bullet}S$$

$$E_{ox}{\bullet}S + S \overset{K_{d,2}}{\rightleftharpoons} E_{ox}{\bullet}S_2$$

Next, we used the kinetic data to determine the net equilibrium constant ($K_{d,net}$) for dissociation of 6-HNA from the tightly bound E_{ox}·S complex. Using eq 9 and the parameters obtained from the hyperbolic fit of k_{obs} values, a $K_{d,net}$ of 0.37 mM was calculated for 6-HNA.

$$K_{d,net} = K_{d,1} + K_{d,1}\left({}^{k_{-2}}/_{k_2}\right) \quad (9)$$

We also estimated the $K_{d,net}$ from the amplitudes of the kinetic traces (ΔA_{450}) since the final A_{450} values represent the absorbance at equilibrium. Surprisingly, these values as a function of substrate concentration (Figure 2C, blue/green diamonds) yielded a significantly lower $K_{d,net}$ (~0.1 mM) compared to that determined from the k_{obs} values. We noted that the ΔA_{450} values began to decrease at substrate concentrations >2 mM instead of stabilizing as expected. We rationalized that the smaller ΔA_{450} (*i.e.*, amplitude) would result in a shorter apparent half-life, and therefore, faster observed rates and a higher apparent $K_{d,net}$. The decrease in ΔA_{450} at high substrate concentrations was confirmed by equilibrium measurements of E_{ox} titrated with 6-HNA at 4 °C (Figure 2C, black/red circles). This static titration also supported a lower estimate of the $K_{d,net}$ of ~0.07 mM from the $K_{1/2max}$, similar to the $K_{d,net}$ determined from the amplitudes of the kinetic traces (Figure 2C). Since both equilibrium measurements indicated a lower $K_{d,net}$ compared to the binding kinetics, we concluded that the analytical kinetic fits do not report on the true $K_{d,1}$, k_2, and k_{-2} constants in a simple two-step binding model.

In order to more accurately estimate the $K_{d,1}$, k_2, and k_{-2} constants for 6-HNA binding, we analyzed the kinetic traces using computer simulation by numerical integration[26] with a more complex binding model. We hypothesized that a second molecule of 6-HNA could bind to form an E_{ox}·S_2 complex with a lower extinction coefficient compared to E_{ox}·S at high substrate concentrations (Scheme 1B). This hypothesis was supported by the observation of substrate inhibition in steady state assays at high concentrations of 6-HNA (Figure S4). Using the two-site binding model, we performed a global simulation of the equilibrium data and time-dependent kinetic traces at four wavelengths: 349, 400, 450, and 476 nm (Figure 2 and Figure S3). This analysis generated best-fit values for the microscopic rate constants for each step (Table 1) and the extinction coefficients for each state in the model (Table S1). As anticipated, the k_2 rate constant was notably lower compared to the analytical solution when accounting for the decrease in A_{450} at high substrate concentrations (Table 1). Indeed, a *FitSpace* analysis[27] of the statistical confidence in each parameter (Figure S5) revealed that, despite being well-constrained by the data, the k_2 rate constant has a slight dependence on the A_{450} extinction coefficient for the E_{ox}·S complex. Although only lower limits could be established for k_1 and k_{-1} according to the *FitSpace* analysis, the ratio of these two rate constants (*i.e.*, the equilibrium constant) was well defined by the data and more than 2-fold lower than the analytical solution (Figure S5). All possible combinations of

Table 1. Equilibrium and Rate Constants for 6-HNA (S) Binding to Oxidized NicC (E_{ox})

reaction	constant	analytical fit	simulation[a]
E_{ox} + S = $*E_{ox}$·S	$K_{d(1)}$	2.3 mM	0.90 mM
$*E_{ox}$·S = E_{ox}·S	k_2	110 s^{-1}	94 s^{-1}
	k_{-2}	21 s^{-1}	15 s^{-1}
E_{ox}·S + S = E_{ox}·S_2	$K_{d(S2)}$	9.3 mM	6.4 mM

[a]Best-fit values based on χ^2 minimization. See the Supporting Information for upper and lower limits of microscopic rate constants determined by *FitSpace* analysis (Figure S5).

https://doi.org/10.1021/acs.biochem.2c00514
Biochemistry 2023, 62, 1553−1567

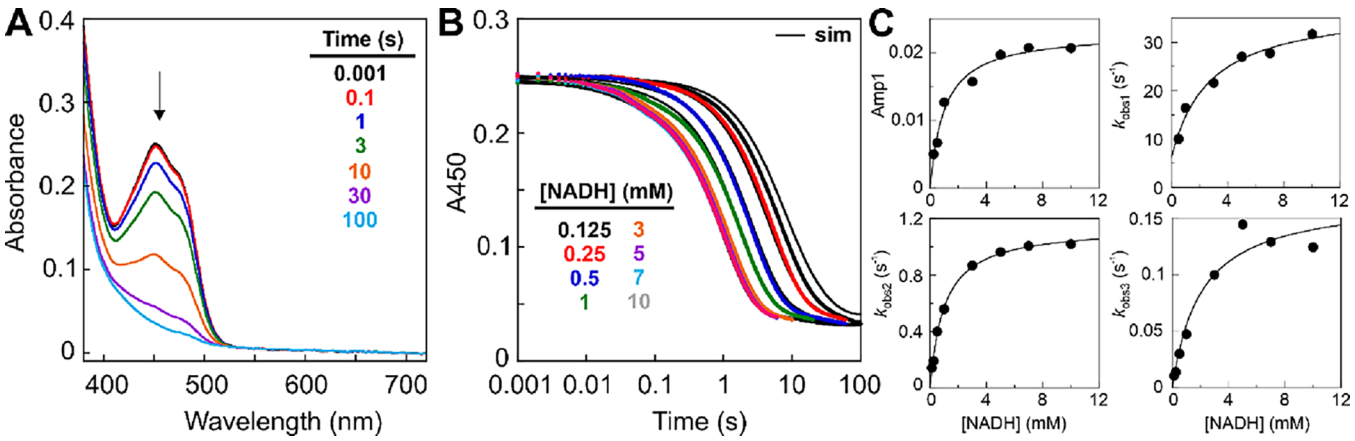

Figure 3. Complex, saturation kinetics describe NADH binding and FAD reduction in the absence of 6-HNA. (A) Absorbance spectra collected over time after mixing a solution of E_{ox} (20 μM final) with an equal volume of NADH (0.125 mM final). (B) A_{450} time-dependent traces from a concentration series in which solutions of NADH (final concentrations listed) were mixed with an equal volume of E_{ox} (20 μM final). Solid black lines represent simulations using the four-step model shown in Scheme 2A. (C) Hyperbolic fits of the NADH-dependence of the amplitude and observed rate constants obtained from analytical fits of the A_{450} time-dependent traces shown in Figure S6.

K_{d1}, k_2, and k_{-2} that exceeded a 95% confidence interval (CI) threshold converged on a $K_{d,net}$ of 0.12 mM for 6-HNA. This net dissociation constant was consistent with a nonlinear regression fit of the equilibrium titration using (eq 1.2) to represent tight binding of 6-HNA to site 1 ($K_{d,net}$ = 0.09 mM) and weak binding of 6-HNA to site 2 ($K_{d,2}$ = 10 mM), respectively (Figure S3).

Altogether, the combination of equilibrium and kinetic measurements of 6-HNA binding to E_{ox} demonstrated weak initial binding followed by a fast second step to form a tighter enzyme−substrate complex. Finally, the data revealed a second, weak affinity binding site for 6-HNA to E_{ox}.

6-HNA Enhances NADH Binding and the Rate of NicC Flavin Reduction. Next, we conducted a set of experiments to probe the effect of 6-HNA on FAD reduction by NADH. Stopped-flow absorption spectroscopy experiments were carried out under anoxic conditions at 4 °C to preclude further reaction of the reduced enzyme with O_2. First, the reduction kinetics were evaluated in the absence of substrate. Rapid mixing of oxidized NicC with NADH resulted in the expected decrease in A_{450} (Figure 3A), indicative of FAD reduction. The A_{450} time-dependent traces from a series of reactions with varying NADH concentrations (Figure 3B) were best fit by nonlinear regression using an equation (eq 4) with three consecutive exponentials (Figure S6). The fit parameters included two small amplitude terms and one large amplitude term (>80% of the total amplitude), the latter likely corresponding to FAD reduction. Analysis of each observed rate constant (k_{obs}) as a function NADH concentration (Figure 3C) revealed non-linear dependence on NADH, suggesting multistep binding of NADH prior to hydride transfer (Scheme 2A). Hyperbolic fits of the k_{obs1} and k_{obs2}, the latter associated with the large amplitude term, yielded equilibrium constants for NADH binding steps and microscopic rate constants for hydride transfer in the forward direction (Table 2). Using eq 9 for a two-step, rapid-equilibrium binding model, a weak $K_{d,net}$ of 0.45 mM was calculated for NADH in the absence of 6-HNA, which is close to 2-fold of the $K_{d,net}$ (1 mM) determined from hyperbolic fits of the first amplitude term and the k_{obs2} as a function of NADH concentration (Figure 3C). The best fit of the k_{obs2} values was achieved by considering an irreversible hydride transfer step, yielding a moderately slow rate constant

Scheme 2. Kinetic Models for the Reductive Half-Reaction in the Absence (A) and Presence (B) of 6-HNA

A No 6-HNA

$$E_{ox} + NADH \underset{k_{-3a}}{\overset{k_{3a}}{\rightleftharpoons}} {}^{*}E_{ox}{\cdot}NADH \underset{k_{-3b}}{\overset{k_{3b}}{\rightleftharpoons}} E_{ox}{\cdot}NADH \underset{k_{-4a}}{\overset{k_{4a}}{\rightleftharpoons}} E_{red}{\cdot}NAD^{+} \underset{k_{-5a}}{\overset{k_{5a}}{\rightleftharpoons}} E_{red} + NAD^{+}$$

B 6-HNA

$$E_{ox}{\cdot}S + NADH \underset{k_{-3}}{\overset{k_{3}}{\rightleftharpoons}} \underset{(CTC)}{E_{ox}{\cdot}S{\cdot}NADH} \underset{k_{-4}}{\overset{k_{4}}{\rightleftharpoons}} E_{red}{\cdot}S{\cdot}NAD^{+} \underset{k_{-5}}{\overset{k_{5}}{\rightleftharpoons}} E_{red}{\cdot}S + NAD^{+}$$

Table 2. Microscopic Rate Constants for NicC (E) Reduction and Oxidation without 6-HNA

modeled reaction	rate constant	analytical fitting	simulation[a]
E_{ox} + NADH = *E_{ox}·NADH	$K_{d(3a)}$	2.7 mM	2.5 mM
*E_{ox}·NADH = E_{ox}·NADH	k_{3b}	31 s^{-1}	59 s^{-1}
	k_{-3b}	6.2 s^{-1}	26 s^{-1}
E_{ox}·NADH = E_{red}·NAD^+	k_{4a}	1.1 s^{-1}	1.5 s^{-1}
	k_{-4a}	0 s^{-1}	0.07 s^{-1}
E_{red}·NAD^+ = E′$_{red}$ + NAD^+	k_{5a}	0.17 s^{-1}	0.07 s^{-1}
	k_{-5a}	nd	<5 $mM^{-1}{\cdot}s^{-1}$
E′$_{red}$ + O_2 → E_{ox} + H_2O_2	k_{6a}	0.8 $mM^{-1}{\cdot}s^{-1}$	0.41 $mM^{-1}{\cdot}s^{-1}$

[a]Best-fit values based on χ^2 minimization. See the Supporting Information for upper and lower limits determined by *FitSpace* analysis (Figure S8).

for reduction (k_{4a} = 1.1 s^{-1}). However, an experiment in which E_{red} was reacted with high concentrations of NAD^+ demonstrated a small extent of FAD oxidation (Figure S7), indicating that hydride transfer is reversible. Based on the observed amplitude (ΔA_{450} = 0.018), we estimate a K_{eq} of 12.9 ± 0.1 for E_{ox}/E_{red}. A similar amplitude (ΔA_{450} = 0.017) was noted in the forward reaction, corresponding to the third kinetic phase (k_{obs3}) following hydride transfer. The decrease in A_{450} (k_{obs3} < 0.15 s^{-1}) was also accompanied by a slow decrease in absorbance at 340 nm (Figure S6), indicating consumption of NADH during this kinetic phase. This slow

https://doi.org/10.1021/acs.biochem.2c00514
Biochemistry 2023, 62, 1553−1567

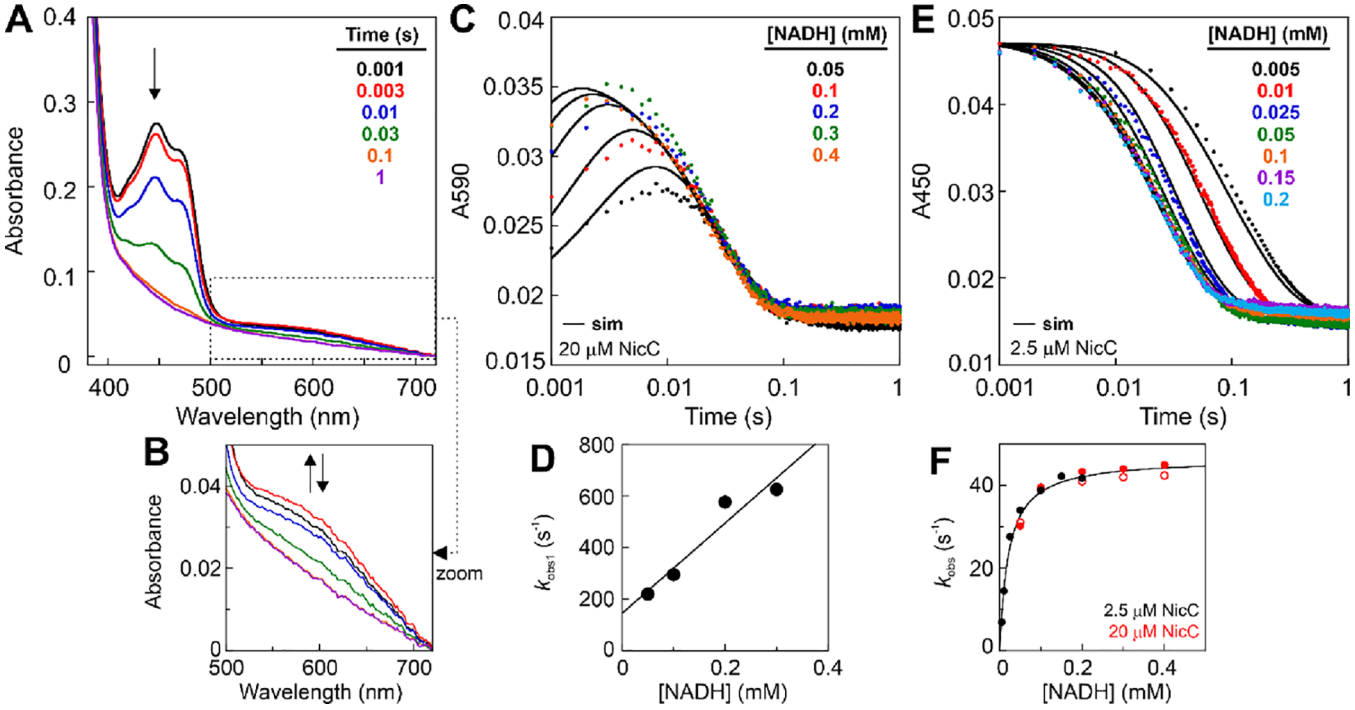

Figure 4. Charge-transfer complex with NADH precedes NicC FAD reduction in the presence of 6-HNA. Substrate and enzyme concentrations listed are final after mixing. (A) Absorbance spectra collected over time of E_{ox} (20 μM) and 6-HNA (1.25 mM) with NADH (0.20 mM). (B) Zoom-in of the 500−700 nm region of the spectra in panel (A). Time-dependent traces of (C) A_{590} with 20 μM E_{ox} and (E) A_{450} with 2.5 μM E_{ox} from two independent concentration series with varying NADH in the presence of 6-HNA (1.25 mM). Solid black lines represent global simulations using the kinetic model in Scheme 2B. (D) Linear NADH-dependence of the observed rates for A_{590} formation (k_{obs1}) obtained from analytical fits shown in Figure S9. (F) Hyperbolic NADH-dependence of the observed rate constants (k_{obs}) obtained from analytical fits (Figure S9) of A_{590} exponential decay (empty circles) and A_{450} exponential decay (filled circles) at low (black) and high (red) NicC concentrations.

reduction phase drives the equilibrium forward to a greater extent, resulting in almost complete reduction of the flavin as shown by the absorbance spectrum at t = 100 s (Figure 3A). These experiments in the absence of 6-HNA revealed a complex kinetic model for NADH binding and reduction that is best described by Scheme 2A, where the slow reduction phase is represented by step 5a.

We then performed global simulation of the NADH concentration series in the absence of 6-HNA to evaluate the model in Scheme 2A. Simulations using a simpler three-step model compared to the complex four-step model in Scheme 2A revealed a better simulation with the four-step model as determined by a lower χ^2 value (normalized by the degrees of freedom) and reduced residuals (Figure S8). In particular, the three-step model was unable to recapitulate a small decrease in absorbance prior to hydride transfer, primarily observed with high concentrations of NADH (Figure S8). The simulation using the four-step model yielded similar constants for NADH binding and hydride transfer as those determined from analytical fits (Table 2) and provided extinction coefficients for each state in the model (Table S1). Additionally, slow rate constants for reverse hydride transfer and the final reduction phase (step 5a) were supported by the data simulation as shown from the *FitSpace* analysis (Figure S8). Overall, the reduction data in the absence of 6-HNA revealed weak binding of NADH and slow FAD reduction that may involve protein conformational changes.

Analogous rapid mixing experiments were conducted at 4 °C with E_{ox} that was pre-incubated with excess 6-HNA (*i.e.*, 10-fold higher than the K_d). When the pre-formed E_{ox}·6-HNA complex was mixed with NADH, a new transient species formed prior to FAD reduction that was not observed in the absence of 6-HNA (Figure 4A). A charge-transfer complex (CTC) with a weak absorption maximum at 590 nm appeared rapidly, mostly within the instrument deadtime (t = 0.001 s), and its accumulation increased (*i.e.*, larger A_{590} amplitude) with higher NADH concentrations (Figure 4B,C). Only a slight decrease in the A_{450} feature was observed during this kinetic phase (Figure S9), indicating that the FAD cofactor remained predominantly oxidized. The A_{590} time-dependent traces were fit by nonlinear regression (Figure S9) with an equation consisting of two exponential functions (eq 5). The observed rate constants for A_{590} formation (k_{obs1}) showed linear dependence on NADH concentration, yielding a second-order rate constant (k_3) of 1.7 × 10^6 M^{-1}·s^{-1} from the slope and a dissociation rate constant (k_{-3}) of 150 s^{-1} from the y-intercept (Figure 4D). However, the fast rate of CTC formation prevented acquisition of sufficient data at early time points, leading to uncertainty in the kinetic constants derived from the analytical solutions.

Decay of the CTC (0.006−0.10 s) was accompanied by a major decrease in absorbance at 450 nm (Figure 4E), corresponding to forward hydride transfer from NADH to FAD. The observed rate constants obtained from analytical fits at both 450 and 590 nm were very similar and showed non-linear dependence on the NADH concentration (Figure 4F). The observed rates appeared to approach a maximum (k_{obs} ≈ 45 s^{-1}) at NADH concentrations lower than observed for the reduction kinetics without 6-HNA. To determine the NADH binding affinity more accurately, a second stopped-flow experiment was conducted with a lower concentration of NicC (2.5 μM final) and excess 6-HNA (*i.e.*, 10-fold higher

https://doi.org/10.1021/acs.biochem.2c00514
Biochemistry 2023, 62, 1553−1567

than the K_d) with a lower range of NADH concentrations. At this enzyme concentration, the CTC could not be detected due to its low extinction coefficient. The A_{450} time-dependent traces were fit by nonlinear regression (Figure S9) using an equation with two exponential functions (eq 5). The NADH-dependence of the observed rate constant (k_{obs1}) for an amplitude change of ∼0.03 was best fit by a hyperbolic function for an irreversible reaction (Figure 4F). This fit yielded a dissociation constant (K_d) for NADH of 21 μM and a rate constant for forward hydride transfer (k_4 = 47 s^{-1}) ((Table 3). The reverse hydride transfer reaction was probed in a

Table 3. Equilibrium and Rate Constants for the Reductive Half-Reaction in the Presence of 6-HNA

reaction	constant	analytical fit	simulation[a]
E_{ox}·S + NADH = E_{ox}·S·NADH	k_3	1.7 $\mu M^{-1}\cdot s^{-1}$	K_d = 3.5 μM
	k_{-3}	150 s^{-1}	
E_{ox}·S·NADH = E_{red}·S·NAD^+	k_4	47 s^{-1}	42 s^{-1}
	k_{-4}	0 s^{-1}	0.2 s^{-1}
E_{red}·S·NAD^+ = E'_{red}·S + NAD^+	k_5	2.1 s^{-1}	>5 s^{-1}
	k_{-5}	nd	<0.33 $\mu M^{-1}\cdot s^{-1}$

[a]Best-fit values based on χ^2 minimization. See the Supporting Information for upper and lower limits determined by *FitSpace* analysis (Figure S10).

separate experiment where E_{red} was preincubated with excess 6-HNA and then mixed with a high concentration of NAD^+. A small increase in absorbance (ΔA_{450} ≈ 0.02) was observed (Figure S7), indicating that hydride transfer is reversible with a similar equilibrium constant as reduction without 6-HNA (K_{eq} ∼ 13). However, no substantial evidence of reversibility could be discerned from the data collected in the forward reaction. Only a very minimal change in A_{450} (∼0.005) with an observed rate constant of 1.8 ± 0.8 s^{-1} was noted with high enzyme concentration following hydride transfer (Figure S9), in contrast to the slow kinetic phase (k_{obs3} ≈ 0.15 s^{-1}) observed without 6-HNA.

To integrate the experiments collected at both enzyme concentrations, we performed a global simulation of the A_{590} and A_{450} time-dependent traces from the NADH concentration series (Figure 4C,E) with a single kinetic model (Scheme 2B). By simultaneously fitting traces at multiple NADH concentrations, the equilibrium constant for NADH binding could be better constrained compared to analytical fits of each trace independently. This global simulation yielded a lower K_d (3.5 μM) for NADH in the presence of 6-HNA and a fast forward rate constant for hydride transfer (k_4 = 42 s^{-1}) with a slow reverse rate constant (k_{-4} = 0.2 s^{-1}) (Table 3). Simulation also enabled an estimate of the extinction coefficients for each state in the model (Table S1). Overall, comparison of the reductive half-reaction datasets showed that the 6-HNA substrate resulted in markedly tighter binding affinity of NADH and a significantly faster rate of forward hydride transfer.

Two Transient Intermediates Accumulate in the Reaction of Reduced NicC with Dioxygen in the Presence of 6-HNA. To study the oxidative half-reaction of NicC with dioxygen, we monitored the spectrum of the flavin cofactor during a single-turnover reaction using rapid-mixing absorption spectroscopy. In these experiments, oxidized NicC was first incubated in the absence of dioxygen with excess 6-HNA and stoichiometric NADH to reduce the flavin, forming the E_{red}·6-HNA complex. This anoxic enzyme solution was then rapidly mixed with O_2-saturated buffer at 4 °C ([O_2] ≈ 1.9 mM) and monitored over 10 s. Evaluation of the time-resolved absorbance spectra revealed three distinct kinetic phases during the reaction with O_2. In the initial 0.06 s, a new species accumulated (Int-I) with a spectrum distinct from the reduced FAD state (Figure 5A, black to red). Int-I displayed a broad spectral feature with an apparent absorbance maximum at 390 nm. This feature disappeared in the second phase of the reaction (0.06−0.25 s), concomitant with accumulation of a second transient species (Int-II) that absorbed maximally at ∼360 nm (Figure 5A, red to blue). In the last phase of the reaction (0.2−3 s), the features of Int-II diminished and the characteristic features of oxidized FAD appeared (λ_1 = 385 nm, λ_2 = 450 nm) (Figure 5A, blue to green). The oxidized FAD features persisted for at least 10 s, signifying the completion of a single turnover due to the absence of excess reductant. When 6-HNA was omitted from the reaction, reduced NicC slowly oxidized (k_{obs} = 0.8 s^{-1}, Figure 5E and Figure S12) without accumulation of Int-I or Int-II (Scheme 3A). Thus, the presence of 6-HNA triggered the formation of Int-I and Int-II, suggesting that they are likely to be relevant catalytic intermediates.

To deconvolute the kinetics of intermediate formation and decay, the time-dependent traces at wavelengths about the absorbance maxima (λ_{max} ± 10 nm) were evaluated for each species. From this analysis, the traces at 400, 349, and 450 nm were selected to represent the kinetics of Int-I, Int-II, and E_{ox}, respectively (Figure 5B). For a more robust kinetic analysis, a series of rapid-mixing experiments was performed with varying concentrations of O_2. The observed rates for the increase in A_{400} (Int-I) and A_{349} (Int-II) demonstrated dependence on the concentration of O_2, whereas the A_{450} signal was minimally influenced (Figure 5 and Figure S14). We first fit the time-dependent traces at each O_2 concentration by nonlinear regression (Figure S14) using equations derived from a kinetic model with three first-order, irreversible steps (eqs 6−8). However, it was difficult to obtain unique microscopic rate constants for each step in the oxidation reaction due to the overlapping absorbance features and comparable apparent rates of formation and decay of the intermediate states. In an effort to alter the kinetics to further resolve intermediate accumulation, the experiment was repeated in the presence of excess sodium azide, a reported inhibitor of other flavin monooxygenases.[28−30] The presence of azide resulted in slower kinetics for all three steps of the oxidative half-reaction but did not reveal any new spectral features (Figure S12).

To overcome these challenges of analytical fitting, we performed a global simulation of the time-dependent traces (A_{400}, A_{349}, and A_{450}) at all O_2 concentrations and one set of time-resolved spectra at the highest O_2 concentration (0.95 mM O_2). The data were simulated according to the kinetic model shown in Scheme 3B, which included an experimentally determined constraint for oxidative uncoupling (*vide infra*). The simulation yielded best-fit values for the microscopic rate constants (Table 4) and extinction coefficients (Table S1) that accurately recapitulated the observed time-dependent traces as a function of O_2 concentration (Figure 5B). The *FitSpace* analysis provided insight into the statistical confidence for these best-fit values (Figure S13). Whereas the rate constant of Int-I formation (k_6 = 36 $mM^{-1}\cdot s^{-1}$) and its extinction coefficients were well-constrained by the data, the rate constants for Int-I (k_7) and Int-II decay (k_8) are inversely dependent on one another (Figure S13). The k_7 and k_8 rate

https://doi.org/10.1021/acs.biochem.2c00514
Biochemistry 2023, 62, 1553−1567

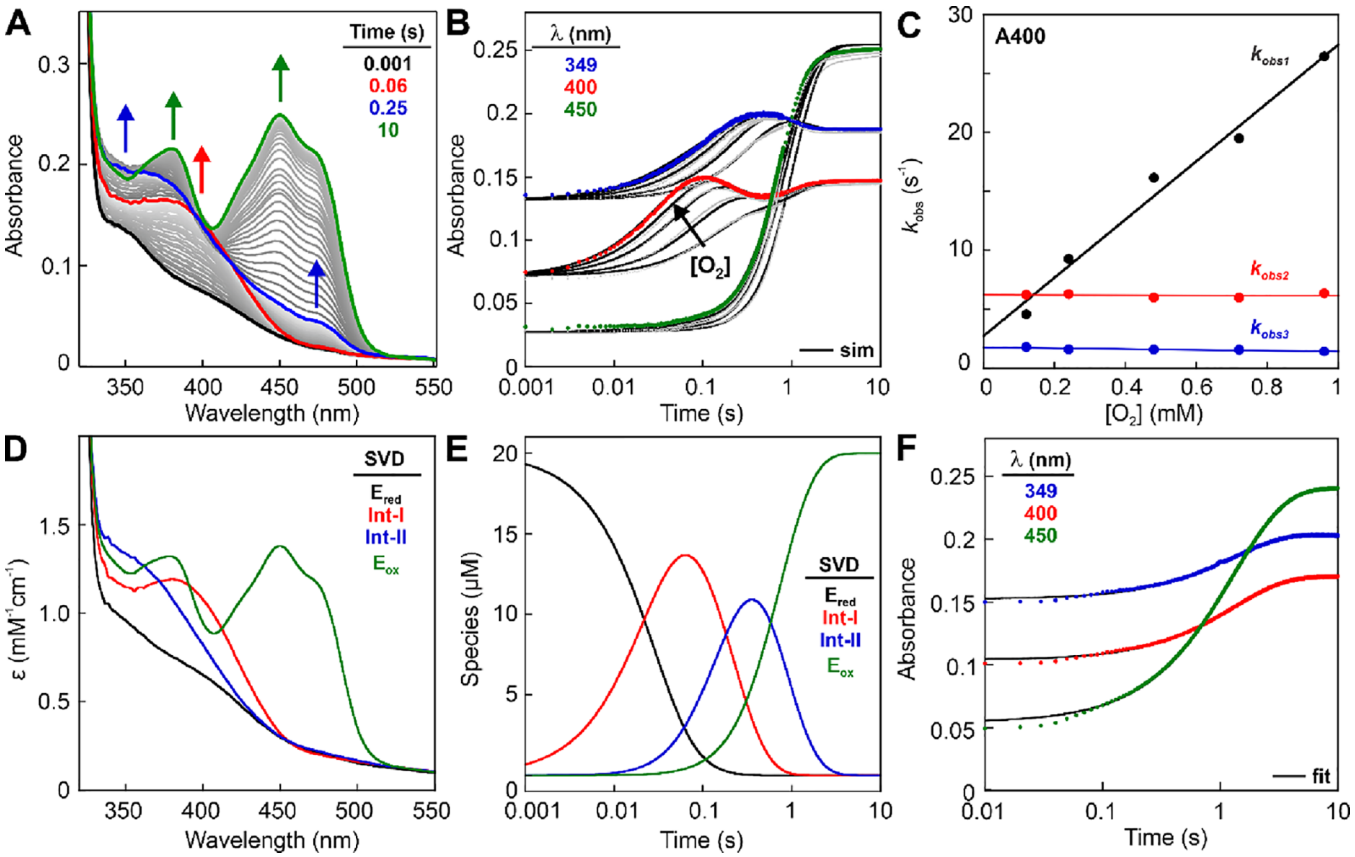

Figure 5. Formation of transient intermediates in the reaction of reduced NicC with O_2 in the presence of 6-HNA. Concentrations listed for substrates and enzyme are final after mixing. (A) Time-dependent absorbance spectra after mixing of an anoxic solution of NicC (18.5 μM), NADH (20 μM), and 6-HNA (1.25 mM) with O_2-saturated (0.95 mM) sodium phosphate buffer (50 mM, pH 7.5) at 4 °C. (B) Time-dependent traces of select wavelengths from the spectra shown in panel (A). Gray points correspond to traces obtained from an O_2 concentration series. Solid black lines represent global simulations using the kinetic model in Scheme 3B. (C) O_2-dependence of the k_{obs} values obtained nonlinear regression fits of the A_{400} time-dependent traces using eq 6 for three first-order irreversible reactions. (D) Spectra of the species determined from singular value decomposition of the time-resolved spectra shown in panel (A). (E) Simulated concentrations of the individual SVD components as a function of time based on the kinetic model in Scheme 3B. (F) Time-dependent traces of select wavelengths from a reaction omitting 6-HNA. Solid black lines are analytical fits with a single exponential equation.

Scheme 3. Kinetic Model for the Oxidative Half-Reaction in the Absence (A) and Presence (B) of 6-HNA

A No 6-HNA

$$E_{red} + O_2 \xrightarrow{k_{6a}} E_{ox} + H_2O_2$$

B 6-HNA

$$E_{red}{\cdot}S + O_2 \underset{k_{-6}}{\overset{k_6}{\rightleftharpoons}} E_{Int\text{-}I}{\cdot}S \xrightarrow{k_7} E_{Int\text{-}II}{\cdot}P \xrightarrow{k_8} E_{ox} + H_2O + P$$

$$E_{Int\text{-}I}{\cdot}S \xrightarrow{k_{7a}} E_{ox}{\cdot}S + H_2O_2$$

Table 4. Equilibrium and Rate Constants for the Oxidative Half-Reaction

reaction	constant	analytical fit	simulation[a]
$E_{red}{\cdot}S + O_2 = E_{HP}{\cdot}S$	k_6	25 $mM^{-1}{\cdot}s^{-1}$	36 $mM^{-1}{\cdot}s^{-1}$
	k_{-6}	2.7 s^{-1}	0 s^{-1}
$E_{Int\text{-}I}{\cdot}S \rightarrow E_{Int\text{-}II}{\cdot}P$	k_7[b]	nd	5.0 s^{-1}
$E_{Int\text{-}II}{\cdot}P \rightarrow E_{ox} + H_2O + P$	k_8	nd	1.6 s^{-1}
$E_{Int\text{-}I}{\cdot}S \rightarrow E_{ox}{\cdot}S + H_2O_2$	k_{7a}[b]	nd	0.45 s^{-1}

[a]Best-fit values based on χ^2 minimization. See the Supporting Information for upper and lower limits determined by *FitSpace* analysis (Figure S13). [b]Rate constants were linked as a 9:1 ratio based on independent experimental results.

constants also showed some dependence on the poorly defined extinction coefficients for Int-II (Figure S13), suggesting multiple statistically plausible combinations of parameters. However, the best-fit values from the simulation with defined upper and lower bounds (Figure S13) support a model with faster Int-I decay (k_7 = 5 s^{-1}) and slower decay of Int-II (k_8 = 1.6 s^{-1}).

Since the final step in the kinetic model represented both product dissociation and cofactor regeneration to the E_{ox} state, we attempted to determine the order of these steps by additional transient and steady-state experiments. We hypothesized that if product dissociation occurred prior to flavin dehydration, then high concentration of 2,5-DHP may slow the rate of dehydration in a single turnover assay. However, the observed rate of dehydration monitored by the increase in A_{450} was unchanged in the presence of 10 mM 2,5-DHP (Figure S12), indicating that (i) product dissociation occurs after flavin dehydration, (ii) product dissociation is very fast relative to dehydration, or (iii) product association is very slow relative to dehydration. Next, we reasoned that if product dissociation occurs from the E_{ox} state, then 2,5-DHP would be

https://doi.org/10.1021/acs.biochem.2c00514
Biochemistry 2023, 62, 1553−1567

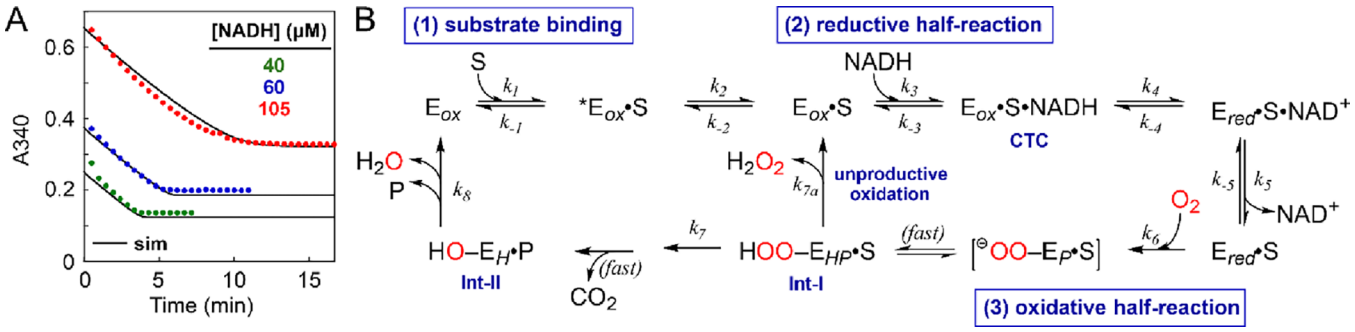

Figure 6. Microscopic rate constants obtained from transient state analysis recapitulate the multiple turnover catalytic rate. (A) Full progress time course of NicC catalysis under multiple turnover conditions (20 nM NicC, 0.1 mM 6-HNA). Solid black line represents the simulated progress curve using the overall kinetic model illustrated in panel (B), rate constants reported in Tables 1−4, and extinction coefficients (ε, $mM^{-1}\cdot cm^{-1}$) at 340 nm for S (0.0133), P (3.31), NADH (6.22), and NAD^+ (0.04).

a competitive or noncompetitive inhibitor of 6-HNA, but not an uncompetitive inhibitor. Steady-state assays with varying 6-HNA concentrations demonstrated a decrease in the $V_{max,app}$ as a function of 2,5-DHP concentration (Figure S15), indicating noncompetitive or mixed inhibition (K_i = 3.7 ± 0.6 mM; K_i' = 6.2 ± 0.6 mM) with respect to 6-HNA. Conversely, steady-state assays with varying NADH concentrations demonstrated an increase in the $K_{M,app}$ but no change in the V_{max}, as a function of 2,5-DHP concentration (Figure S15), indicating competitive inhibition (K_i = 1.2 ± 0.4 mM) with respect to NADH. These results suggest a kinetic model where the 2,5-DHP product binds to both the E_{ox} and E_{ox}·S states, suggesting that cofactor regeneration precedes product dissociation. However, since product dissociation lacks a sufficient spectroscopic handle (Figure S16), we concluded that the kinetics of the oxidative half-reaction are best represented by Scheme 3B with one combined step for flavin regeneration and product dissociation.

Singular value decomposition of the time-dependent spectra using this kinetic model resolved four components (Figure 5D), representing E_{red}·S (black), Int-I (red), Int-II (blue), and E_{ox}·S (green). The calculated spectrum of Int-I closely matched the experimental spectrum at t = 0.06 s; however, the calculated and experimental (t = 0.25 s) spectra for Int-II were notably different. While the intense feature at 360 nm is apparent in both spectra for Int-II, the experimental spectrum of Int-II also showed absorbance at 475 nm (Figure 5A, blue). As C4a-adducts do not typically absorb at longer wavelengths (>400 nm) (Table S2), this feature indicated E_{ox} formation on the same timescale as Int-II formation and Int-I decay. Flavin monooxygenases are well-documented to unproductively generate H_2O_2 upon decay of C4a-oxygen adducts to FAD without substrate hydroxylation.[15] To assess the extent of unproductive decay of Int-I to E_{ox}, we determined the coupling between substrate hydroxylation and NADH consumption in a single-turnover endpoint assay under conditions identical to the rapid-mixing experiment with 0.95 mM O_2. Quantification of 2,5-DHP by high-performance liquid chromatography (UV/vis) revealed a ratio of 0.905 (± 0.002) molar equivalents of 2,5-DHP to 1 molar equivalent of NADH. A fluorescence assay was also performed to detect H_2O_2, which determined 0.096 (±0.02) molar equivalents of H_2O_2 to 1 molar equivalent of NADH. This minimal uncoupling (~10%) is insufficient to account for the observed absorbance intensity at 475 nm contributed by E_{ox} at t = 0.25 s. Rather, the similar rate constants for Int-II formation and decay result in simultaneous observation of E_{ox} at the time of maximal Int-II accumulation (t = 0.25 s), as depicted in terms of species concentration in Figure 5E.

Transient State Kinetic Model and Parameters Reproduce the Observed Steady-State Catalytic Rate. Finally, we evaluated whether the global kinetic model was consistent with the overall rate of catalysis at 4 °C under steady-state conditions. Multiple-turnover assays with varying NADH concentrations in the presence and absence of 6-HNA were monitored to completion by measuring the absorbance at 340 nm (A_{340}) (Figure 6A and Figure S17), which reflects NADH depletion (ε_{340} = 6.22 $mM^{-1}\cdot cm^{-1}$) and 2,5-DHP production (ε_{340} = 3.31 $mM^{-1}\cdot cm^{-1}$). The turnover number ($\nu/[E_0]$) at 4 °C in the presence of 6-HNA was 1.3 ± 0.5 s^{-1} compared to 0.20 ± 0.01 s^{-1} in the absence of substrate. We also performed a control measuring the rate of NADH decomposition in buffer (k_{obs} = 1.2 × 10^{-5} s^{-1}) to include in the simulation (Figure S17). A global simulation using the kinetic parameters determined in this work (Tables 1−4) accurately recapitulated the full progress time course data with and without substrate under multiple-turnover conditions at multiple concentrations of NADH (Figure 6A and Figure S17). The accuracy of the simulation was strongly influenced by the microscopic rate constants for NAD^+ dissociation (k_5), as well as the rate constant for Int-I (k_7) and Int-II decay (k_8), indicating that these steps are partially rate-limiting in catalysis.

DISCUSSION

Flavin-dependent monooxygenases are a diverse class of enzymes performing aromatic hydroxylation reactions with exquisite substrate specificity and regioselectivity. A better understanding of the mechanistic features that promote reactivity would provide insight into their biocatalytic potential. In particular, NicC represents a small group of enzymes that catalyze both hydroxylation and C−C bond cleavage of pyridinolic substrates, which have been understudied by comparison to other flavin monooxygenases. We report a detailed spectroscopic and kinetic characterization of all three segments of the NicC catalytic mechanism, including (1) 6-HNA binding, (2) flavin reduction by NADH, and (3) flavin oxidation with substrate hydroxylation. The results of this work are consistent with the overall kinetic model for productive catalysis shown in Figure 6 and highlight the mechanistic features unique to NicC.

The binding kinetics reveal a functional preference for ordered sequential binding of two of the substrates (6-HNA

https://doi.org/10.1021/acs.biochem.2c00514
Biochemistry 2023, 62, 1553−1567

and NADH) to NicC. In the resting oxidized state (E_{ox}), NicC can form weak binary complexes with both 6-HNA and NADH, implying a possible random sequential bi bi mechanism. However, the dissociation constant for 6-HNA is at least 6-fold lower than that of NADH, suggesting a preference for ordered binding. Although the initial binary 6-HNA complex is in rapid equilibrium with substrate-free E_{ox} (K_{d1} = 0.9 mM), the affinity for 6-HNA is enhanced 7.5-fold by an 'isomerization' step after substrate association ($K_{d,net}$ = 0.12 mM). The second step in the substrate binding model may involve ionization of 6-HNA and/or a conformational change of the flavin cofactor. Deprotonation of aromatic substrates is a common feature in flavin monooxygenases that influences substrate binding affinity and selectivity.[31−37] Previous studies of NicC also support a proposed role for ionization in 6-HNA binding. First, NicC has a stronger affinity for the substrate analogue 5-chloro-6-hydroxynicotinate with a lower pyridinolic pK_a than 6-HNA.[13] Second, alanine substitutions of the active site residues His47 and Tyr215, which are predicted to promote and stabilize the ionized form of 6-HNA, demonstrate significantly reduced affinity for 6-HNA and cause uncoupling of NADH oxidation from substrate hydroxylation.[13] Substrate ionization in other flavin monooxygenases is often associated with structural rearrangements of the active site that shift the equilibrium position of the flavin from an "in" (more buried position) to an "out" conformation accessible to NADH.[37] In the case of NicC, the greater extinction coefficient of the flavin at 450 nm observed for the final E_{ox}·S complex compared to substrate-free E_{ox} is consistent with a change in the local flavin environment.

The kinetics of the reductive half-reaction reveal that 6-HNA binding to NicC promotes flavin reduction via increased NADH affinity and accelerated hydride transfer. Class A flavin-dependent aromatic monooxygenases are considered "cautious hydroxylases"[38] because flavin reduction is greatly enhanced by the presence of the aromatic substrate. This substrate triggering mechanism serves to reduce unproductive depletion of cellular NAD(P)H levels and prevents hydrogen peroxide generation when substrate is not available. For most class A monooxygenases, the aromatic substrate influences FAD reduction by substantially increasing the rate of hydride transfer without drastically affecting the enzyme's affinity for NAD(P)H (Table S3). In contrast, two unique features of NicC reduction kinetics emerge from this study. First, NicC is the least effective at preventing unproductive oxidization of NADH in the absence of its substrate. Only the pyridinolic monooxygenase HspB[22] approaches the relatively fast rate of hydride transfer observed for NicC in the absence of substrate (k_{4a} = 1−1.5 s^{-1}). Second, instead of dramatically enhancing the rate of hydride transfer, the primary effect of 6-HNA on NicC reduction is an increase in the affinity for NADH (Figure 7). The presence of 6-HNA lowers the K_d for NADH by 220-fold, which is, to our knowledge, the largest reported enhancement in NAD(P)H affinity for a class A flavin monooxygenase (Table S3). Conversely, substrate binding to NicC has the smallest reported effect on hydride transfer (Table S3), resulting in only a 28-fold increase compared to a 170,000-fold difference for PHBH.[39] However, the accumulation of a charge-transfer complex (CTC)[40] in the presence of the NicC substrate indicates that 6-HNA induces close interaction between oxidized FAD and NADH.[41,42] This interaction may be promoted by the flavin reorientation to the "out" conformation upon substrate ionization, as noted above,

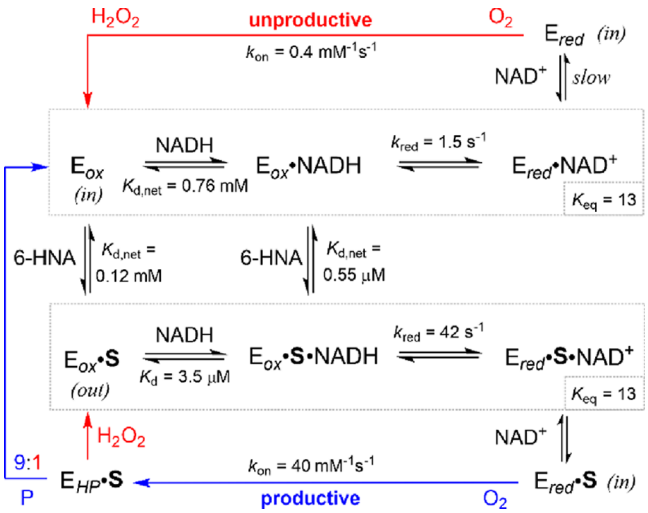

Figure 7. Thermodynamic cycle for substrate binding and reduction depicts a mechanism that suppresses unproductive pathways. All constants were determined experimentally by simulation (Tables 1−2), whereas the $K_{d,net}$ of 6-HNA from E_{ox}·S·NADH was calculated based on the thermodynamic cycle.

enabling more efficient hydride transfer in the ternary complex.[43] Altogether, the combined effects of substrate binding to NicC result in an overall enhancement of the reduction kinetics by a factor of 6.2 × 10^3, which is within the typical range for flavin monooxygenases (Table S3). In the absence of structural evidence, results of the kinetic investigation of NicC suggest that conformational dynamics of both the protein and coenzyme are important for controlling the rate of FAD reduction by NADH at the active site.

The presence of substrate also markedly accelerates the reactivity of reduced NicC toward O_2 by 100-fold and promotes accumulation of catalytic intermediates. The canonical mechanism for class A flavin-dependent aromatic hydroxylases invokes a C4a-hydroperoxy-flavin intermediate (E_{HP}) as the electrophile in an electrophilic aromatic substitution (Figure 8). The transfer of the terminal hydroxyl group of the C4a-hydroperoxy-flavin species results in substrate hydroxylation and generates a C4a-hydroxy-flavin (E_H) intermediate (Figure 8). In single-turnover reactions of reduced NicC with dioxygen, two transient species (Int-I and Int-II) are observed in the presence of 6-HNA that are consistent with the proposed C4a-hydroperoxy-FAD and C4a-hydroxy-FAD intermediates, respectively. The absorbance maximum of Int-I is within the range (380−395 nm) of previously reported C4a-hydroperoxy-FAD flavoenzyme intermediates (Table S2). In contrast, the anionic C4a-peroxy-FAD state (E_P) invoked in nucleophilic flavoenzyme mechanisms has an absorbance maximum at lower wavelengths (∼ 360 nm).[44] The observed rate of Int-I formation in the NicC reaction shows a linear dependence on the concentration of O_2, suggesting that protonation is too fast to allow for accumulation of a discrete C4a-peroxy-FAD intermediate. Compared to Int-I, the absorbance maximum of Int-II is blue-shifted to ∼350 nm, which is consistent with reports of C4a-hydroxy-FAD intermediates in other flavin monooxygenases (Table S2). The spectroscopic elucidation of the C4a-hydroxy-FAD intermediate in other enzymes has sometimes required the addition of inhibitors, such as chloride or azide, to slow down the dehydration step. However, the intrinsic decay of

https://doi.org/10.1021/acs.biochem.2c00514
Biochemistry 2023, 62, 1553−1567

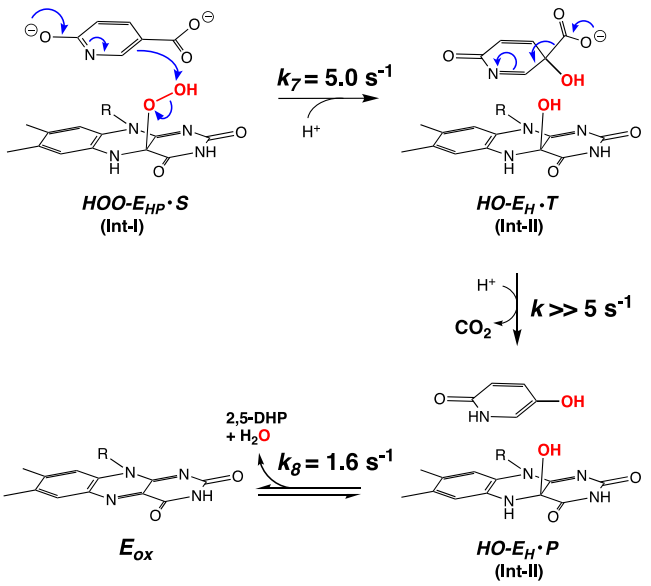

Figure 8. Proposed mechanism for 6-HNA hydroxylation by the C4a-hydroperoxy-flavin intermediate (Int-I) followed by fast decarboxylation of the tetrahedral intermediate (T) to 2,5-dihydroxypyridine and its subsequent dissociation and flavin dehydration.

this intermediate in NicC is remarkably slow (k_8 = 1.6 s^{-1}), permitting its direct detection in the absence of inhibitors. Using singular value decomposition, we were able to elucidate the spectrum of each C4a-intermediate. The spectrum of the C4a-hydroxy-FAD intermediate is particularly difficult to elucidate from experimental spectra, even with the use of inhibitors, because oxidized FAD usually appears on a similar timescale. This observation has been interpreted somtimes to arise from bifurcation of E_{HP} decay via productive substrate hydroxylation to generate E_H and unproductive hydrogen peroxide generation to form E_{ox}. However, independent measurements of the NicC reaction uncoupling demonstrate that the small fraction of unproductive events (10%) do not support this model. Instead, simulations reveal that the simultaneous observation of E_H and E_{ox} spectra is largely due to similar rate constants for E_H formation and decay in the case of NicC.

The observation of kinetically resolved E_{HP} and E_H C4a-intermediates provides important insight into the transformation of the substrate to product and the regeneration of the oxidized FAD quinone form. The oxidative half-reaction of NicC is slow relative to other reported class A flavin monooxygenases (Table S4), including HspB, which also catalyzes *para*-hydroxylation and *ipso*-substitution of a pyridinolic substrate.[22] However, the kinetics of individual steps in the oxidative half-reaction of HspB have not yet been fully elucidated. In NicC, the decay of E_{HP} and formation of E_H report directly on the rate constant for substrate hydroxylation (k_7). However, two other kinetic steps are masked by our data: (1) decarboxylation of the hydroxylated substrate intermediate and (2) product dissociation. The final product, 2,5-DHP, has a significantly lower extinction coefficient (ε_{349} = 0.410 mM^{-1} cm^{-1}) compared to the E_H species (ε_{349} = 10.2 mM^{-1} cm^{-1}), preventing its detection spectroscopically during the oxidative half-reaction. However, we previously determined an inverse $^{13}V/K$ kinetic isotope effect on C−C bond cleavage from the $^{13}C/^{12}C$ ratio in product CO_2.[13] This observation indicates that decarboxylation of the tetrahedral intermediate is faster than its rate of formation, putting a lower limit on the rate of decarboxylation of >5 s^{-1}. Following substrate conversion to product, our results suggest fast product dissociation and slow dehydration of the E_H species to regenerate E_{ox}. However, the order of these steps could not be elucidated. The transient and steady-state assays probing product inhibition demonstrated weak binding affinity for 2,5-DHP, suggesting a plausible role for the C6-carboxylate in substrate recognition and binding. This conclusion is in accord with the weak kinetic inhibition (K_i = 3 mM) observed earlier for NicC with 6-hydroxynicotinaldehyde.[10] Finally, the global simulation of steady-state catalysis using the microscopic rate constants and binding equilibria determined from transient state experiments revealed that substrate hydroxylation and C4a-hydroxy-FAD dehydration are important rate-limiting steps in catalysis. Both individual rate constants exceed the steady-state turnover number ($v/[E_0]$ = 1.3 s^{-1} at 4 °C) as expected, but the combination of the two constants approximates the catalytic rate according to eq 10, indicating that these steps have the most appreciable residence times following substrate binding.

$$k_{cat} = \frac{k_7 k_8}{k_7 + k_8} \tag{10}$$

In conclusion, this study advances our mechanistic understanding of flavin-dependent decarboxylative hydroxylation of pyridinolic substrates, establishing intermediate states and inherent rate constants through global simulation. The results reveal interesting mechanistic distinctions within the broad family of class A monooxygenases and provide a basis for understanding and optimizing NicC catalysis with alternative NHAC substrates in future studies.

■ ASSOCIATED CONTENT

Supporting Information

The Supporting Information is available free of charge at https://pubs.acs.org/doi/10.1021/acs.biochem.2c00514.

Extinction coefficients used in kinetic simulations; UV−visible spectra of the enzyme, substrate, and product; nonlinear regression analysis of transient state kinetics; *FitSpace* analysis from kinetic simulations; steady state kinetics of substrate and product inhibition (PDF)

Accession Codes

NicC UniProtKB entry A0A0H3LKL4

■ AUTHOR INFORMATION

Corresponding Authors

Lauren J. Rajakovich − *Department of Chemistry, University of Washington, Seattle, Washington 98195, United States;* orcid.org/0000-0001-5412-1981; Email: ljraj@uw.edu

Mark J. Snider − *Department of Chemistry, The College of Wooster, Wooster, Ohio 44691, United States;* orcid.org/0000-0003-1054-1276; Email: msnider@wooster.edu

Authors

Scott W. Perkins − *Department of Chemistry, The College of Wooster, Wooster, Ohio 44691, United States*

May Z. Hlaing − *Department of Chemistry, The College of Wooster, Wooster, Ohio 44691, United States*

Katherine A. Hicks − *Department of Chemistry, The State University of New York College at Cortland, Cortland, New York 13045, United States;* orcid.org/0000-0002-1474-1067

https://doi.org/10.1021/acs.biochem.2c00514
Biochemistry 2023, 62, 1553−1567

Complete contact information is available at:
https://pubs.acs.org/10.1021/acs.biochem.2c00514

Author Contributions

The project was conceived by K.A.H. and M.J.S. L.J.R. and M.J.S. designed the experiments. S.W.P. and M.J.S. performed the stopped-flow kinetics experiments. M.Z.H. and M.J.S. performed and analyzed the steady state experiments. S.W.P., M.J.S., and L.J.R. analyzed the transient kinetic data, with L.J.R. leading the data analysis by simulation. The manuscript was written by M.J.S. and L.J.R., with contributions from all authors. All authors have given approval to the final version of the manuscript.

Funding

This work was funded by the National Science Foundation (MCB 1817535 to M.J.S. and 1817633 to K.A.H.).

Notes

The authors declare no competing financial interest.

■ ACKNOWLEDGMENTS

The authors gratefully acknowledge Professors David Ballou (University of Michigan) and J. Martin Bollinger Jr. (Pennsylvania State University) for providing initial guidance and support at the early stages of this work and to Professor Kenneth Johnson (University of Texas at Austin) whose *New Enzymology Kinetics Workshop* inspired M.J.S. and L.J.R. to do kinetic analyses by simulation.

■ ABBREVIATIONS

CTC, charge transfer complex; 2,5-DHP, 2,5-dihydroxypyridine; DTT, dithiothreitol; E_{HP}, C4A hydroxyperoxy-flavin enzyme; E_H, C4A hydroxy-flavin enzyme; E_P, C4A peroxy-flavin enzyme; E_{red}, reduced flavin enzyme state; E_{ox}, oxidized flavin enzyme state; FAD, flavin adenine dinucleotide; 6-HNA, 6-hydroxynicotinate; HspB, 6-hydroxy-3-succinoyl-pyridine 3-monooxygenase; Int-I, intermediate 1; Int-II, intermediate 2; K_d, dissociation equilibrium constant; NAD(P)H, nicotinamide adenine dinucleotide (reduced); $NAD(P)^+$, nicotinamide adenine dinucleotide (oxidized); *N*HACs, *N*-heterocyclic aromatic compound; NicC, 6-hydroxynicotinate 3-monooxygenase; MHPCO, 2-methyl-3-hydroxypyridine-5-carboxylate oxygenase; PHBH, *para*-hydroxybenzoate hydroxylase; $^{13}V/K$, $^{13}C/^{12}C$ kinetic isotope effect on catalytic efficiency

■ REFERENCES

(1) Padoley, K. v.; Mudliar, S. N.; Pandey, R. A. Heterocyclic nitrogenous pollutants in the environment and their treatment options - An overview. *Bioresour. Technol.* **2008**, *99*, 4029−4043.
(2) Barnes, K. K.; Kolpin, D. W.; Furlong, E. T.; Zaugg, S. D.; Meyer, M. T.; Barber, L. B. A national reconnaissance of pharmaceuticals and other organic wastewater contaminants in the United States - I Groundwater. *Sci. Total Environ.* **2008**, *402*, 192−200.
(3) Fetzner, S. Bacterial degradation of pyridine, indole, quinoline, and their derivatives under different redox conditions. *Appl. Microbiol. Biotechnol.* **1998**, *49*, 237−250.
(4) Kaiser, J. P.; Feng, Y.; Bollag, J. M. Microbial metabolism of pyridine, quinoline, acridine, and their derivatives under aerobic and anaerobic conditions. *Microbiol. Rev.* **1996**, *60*, 483−498.
(5) Sims, G. K.; O'Loughlin, E. J.; Crawford, R. L. Degradation of pyridines in the environment. *Crit. Rev. Environ. Sci. Technol.* **1989**, *19*, 309−340.
(6) Behrman, E. J.; Stanier, R. Y. The Bacterial Oxidation of Nicotinic Acid. *J. Biol. Chem.* **1957**, *228*, 923−945.
(7) Jiménez, J. I.; Canales, A.; Jiménez-Barbero, J.; Ginalski, K.; Rychlewski, L.; García, J. L.; Díaz, E. Deciphering the genetic determinants for aerobic nicotinic acid degradation: the nic cluster from *Pseudomonas putida* KT2440. *Proc. Natl. Acad. Sci. U. S. A.* **2008**, *105*, 11329−11334.
(8) Kincaid, V. A.; Sullivan, E. D.; Klein, R. D.; Noel, J. W.; Rowlett, R. S.; Snider, M. J. Structure and catalytic mechanism of nicotinate (vitamin B3) degradative enzyme maleamate amidohydrolase from *Bordetella bronchiseptica* RB50. *Biochemistry* **2012**, *51*, 545−554.
(9) Yao, Y.; Tang, H.; Ren, H.; Yu, H.; Wang, L.; Zhang, W.; Behrman, E. J.; Xu, P. Iron(II)-dependent dioxygenase and *N*-formylamide deformylase catalyze the reactions from 5-hydroxy-2-pyridone to maleamate. *Sci. Rep.* **2013**, *3*, 1−10.
(10) Hicks, K. A.; Yuen, M. E.; Zhen, W. F.; Gerwig, T. J.; Story, R. W.; Kopp, M. C.; Snider, M. J. Structural and biochemical characterization of 6-hydroxynicotinic acid 3-monooxygenase, a novel decarboxylative hydroxylase involved in aerobic nicotinate degradation. *Biochemistry* **2016**, *55*, 3432−3446.
(11) Huijbers, M. M. E.; Montersino, S.; Westphal, A. H.; Tischler, D.; van Berkel, W. J. H. Flavin dependent monooxygenases. *Arch. Biochem. Biophys.* **2014**, *544*, 2−7.
(12) Díaz, E. Bacterial degradation of aromatic pollutants: A paradigm of metabolic versatility. *Int. Microbiol.* **2004**, *7*, 173−180.
(13) Nakamoto, K. D.; Perkins, S. W.; Campbell, R. G.; Bauerle, M. R.; Gerwig, T. J.; Gerislioglu, S.; Wesdemiotis, C.; Anderson, M. A.; Hicks, K. A.; Snider, M. J. Mechanism of 6-hydroxynicotinate 3-monooxygenase, a flavin-dependent decarboxylative hydroxylase involved in bacterial nicotinic acid degradation. *Biochemistry* **2019**, *58*, 1751−1763.
(14) Ballou, D. P.; Entsch, B. The reaction mechanisms of groups A and B flavoprotein monooxygenases. In *Handbook of Flavoproteins: Complex Flavoproteins, Dehydrogenases and Physical Methods*; Walter de Gruyter, 2013, 1−28.
(15) Romero, E.; Gómez Castellanos, J. R.; Gadda, G.; Fraaije, M. W.; Mattevi, A. Same substrate, many reactions: oxygen activation in flavoenzymes. *Chem. Rev.* **2018**, *118*, 1742−1769.
(16) Chenprakhon, P.; Wongnate, T.; Chaiyen, P. Monooxygenation of aromatic compounds by flavin-dependent monooxygenases. *Protein Sci.* **2019**, *28*, 8−29.
(17) Crozier-Reabe, K.; Moran, G. R. Form follows function: Structural and catalytic variation in the class a flavoprotein monooxygenases. *Int. J. Mol. Sci.* **2012**, *13*, 15601−15639.
(18) Paul, C. E.; Eggerichs, D.; Westphal, A. H.; Tischler, D.; van Berkel, W. J. H. Flavoprotein monooxygenases: Versatile biocatalysts. *Biotechnol. Adv.* **2021**, *51*, No. 107712.
(19) Reis, R. A. G.; Li, H.; Johnson, M.; Sobrado, P. New frontiers in flavin-dependent monooxygenases. *Arch. Biochem. Biophys.* **2021**, *699*, No. 108765.
(20) Palfey, B. A. New Approaches for Flavin Catalysis. *Methods Enzymol.* **2019**, *620*, 2−544.
(21) Qiu, J.; Liu, B.; Zhao, L.; Zhang, Y.; Cheng, D.; Yan, X.; Jiang, J.; Hong, Q.; He, J. The novel monocomponent fad-dependent monooxygenase HpaM catalyzes the 2-decarboxylative hydroxylation of 5-hydroxypicolinic acid in *Alcaligenes faecalis* JQ135. *bioRxiv* **2017**, No. 171595.
(22) Yu, H.; Hausinger, R. P.; Tang, H. Z.; Xu, P. Mechanism of the 6-hydroxy-3-succinoyl-pyridine 3-monooxygenase flavoprotein from *Pseudomonas putida* S16. *J. Biol. Chem.* **2014**, *289*, 29158−29170.
(23) Chaiyen, P.; Brissette, P.; Ballou, D. P.; Massey, V. Unusual mechanism of oxygen atom transfer and product rearrangement in the catalytic reaction of 2-methyl-3-hydroxypyridine-5-carboxylic acid oxygenase. *Biochemistry* **1997**, *36*, 8060−8070.
(24) T Greenhagen, B.; Shi, K.; Robinson, H.; Gamage, S.; K Bera, A.; E Ladner, J.; F Parsons, J. Crystal structure of the pyocyanin biosynthetic protein PhzS. *Biochemistry* **2008**, *47*, 5281−5289.
(25) Časaitė, V.; Sadauskas, M.; Vaitekūnas, J.; Gasparavičiūtė, R.; Meškienė, R.; Skikaitė, I.; Sakalauskas, M.; Jakubovska, J.; Tauraitė, D.; Meškys, R. Engineering of a chromogenic enzyme screening

system based on an auxiliary indole-3-carboxylic acid monooxygenase. *MicrobiologyOpen* **2019**, *8*, No. e795.
(26) Johnson, K. A.; Simpson, Z. B.; Blom, T. Global Kinetic Explorer: A new computer program for dynamic simulation and fitting of kinetic data. *Anal. Biochem.* **2009**, *387*, 20−29.
(27) Johnson, K. A.; Simpson, Z. B.; Blom, T. FitSpace Explorer: An algorithm to evaluate multidimensional parameter space in fitting kinetic data. *Anal. Biochem.* **2009**, *387*, 30−41.
(28) Entsch, B.; Ballou, D. P.; Massey, V. Flavin oxygen derivatives involved in hydroxylation by p hydroxybenzoate hydroxylase. *J. Biol. Chem.* **1976**, *251*, 2550−2563.
(29) Sucharitakul, J.; Tongsook, C.; Pakotiprapha, D.; van Berkel, W. J. H.; Chaiyen, P. The reaction kinetics of 3-hydroxybenzoate 6-hydroxylase from *Rhodococcus jostii* RHA1 provide an understanding of the para-hydroxylation enzyme catalytic cycle. *J. Biol. Chem.* **2013**, *288*, 35222−35221.
(30) Powlowski, J.; Ballou, D. P.; Massey, V. Studies of the oxidative half-reaction of anthranilate hydroxylase (deaminating) with native and modified substrates. *J. Biol. Chem.* **1990**, *265*, 4969−4975.
(31) van Berkel, W. J. H.; Müller, F. The temperature and pH dependence of some properties of p-hydroxybenzoate hydroxylase from *Pseudomonas fluorescens*. *Eur. J. Biochem.* **1989**, *179*, 307−314.
(32) Luanloet, T.; Sucharitakul, J.; Chaiyen, P. Selectivity of substrate binding and ionization of 2-methyl-3-hydroxypyridine-5-carboxylic acid oxygenase. *FEBS J.* **2015**, *282*, 3107−3125.
(33) Wang, X.; Hou, Q.; Liu, Y. Insights into the decarboxylative hydroxylation of salicylate catalyzed by the Flavin-dependent monooxygenase salicylate hydroxylase. *Theor. Chem. Acc.* **2018**, *137*, 89.
(34) Eppink, M. H. M.; Boeren, S. A.; Vervoort, J.; van Berkel, W. J. H. Purification and properties of 4-hydroxybenzoate 1-hydroxylase (decarboxylating), a novel flavin adenine dinucleotide-dependent monooxygenase from *Candida parapsilosis* CBS604. *J. Bacteriol.* **1997**, *179*, 6680−6687.
(35) Chaiyen, P.; Brissette, P.; Ballou, D. P.; Massey, V. Reaction of 2-methyl-3-hydroxypyridine-5-carboxylic acid (MHPC) oxygenase with *N*-methyl-5-hydroxynicotinic acid: studies on the mode of binding, and protonation status of the substrate. *Biochemistry* **1997**, *36*, 13856−13864.
(36) Pitsawong, W.; Chenprakhon, P.; Dhammaraj, T.; Medhanavyn, D.; Sucharitakul, J.; Tongsook, C.; van Berkel, W. J. H.; Chaiyen, P.; Miller, A. F.; Banerjee, R. Tuning of p*Ka* values activates substrates in flavin-dependent aromatic hydroxylases. *J. Biol. Chem.* **2020**, *295*, 3965−3981.
(37) Palfey, B. A.; Moran, G. R.; Entsch, B.; Ballou, D. P.; Massey, V. Substrate recognition by "password" in p-hydroxybenzoate hydroxylase. *Biochemistry* **1999**, *38*, 1153−1158.
(38) Palfey, B. A.; McDonald, C. A. Control of catalysis in flavin-dependent monooxygenases. *Arch. Biochem. Biophys.* **2010**, *493*, 26−36.
(39) Husain, M.; Massey, V. Kinetic studies on the reaction of p-hydroxybenzoate hydroxylase. Agreement of steady state and rapid reaction data. *J. Biol. Chem.* **1979**, *254*, 6657−6666.
(40) Howell, L. G.; Spector, T.; Massey, V. Purification and properties of p-hydroxybenzoate hydroxylase from *Pseudomonas fluorescens*. *J. Biol. Chem.* **1972**, *247*, 4340−4350.
(41) Sucharitakul, J.; Wongnate, T.; Montersino, S.; van Berkel, W. J. H.; Chaiyen, P. Reduction kinetics of 3-hydroxybenzoate 6-hydroxylase from *Rhodococcus jostii RHA1*. *Biochemistry* **2012**, *51*, 4309−4321.
(42) Zheng, Y.; Wagner, M. A.; Jorns, M. S.; Carey, P. R. Selective enhancement of ligand and flavin Raman modes in charge-transfer complexes of sarcosine oxidase. *J. Raman Spectrosc.* **2001**, *32*, 79−92.
(43) Wang, J.; Ortiz-Maldonado, M.; Entsch, B.; Massey, V.; Ballou, D.; Gatti, D. L. Protein and ligand dynamics in 4-hydroxybenzoate hydroxylase. *Proc. Natl. Acad. Sci. U. S. A.* **2002**, *99*, 608−613.
(44) Sheng, D.; Ballou, D. P.; Massey, V. Mechanistic studies of cyclohexanone monooxygenase: Chemical properties of intermediates involved in catalysis. *Biochemistry* **2001**, *40*, 11156−11167.

https://doi.org/10.1021/acs.biochem.2c00514
Biochemistry 2023, 62, 1553−1567